The Fabrication and Physics of High-Efficiency CdTe Thin-Film Solar Cells

Annual Technical Report for the Period

September 1, 2002 to August 31, 2003

Contract No. NDJ-1-30630-02

Alvin D. Compaan, principal investigator

Victor Karpov, co-principal investigator

Randy G. Bohn, co-investigator

Dean Giolando, co-investigator

Xunming Deng, co-investigator

NREL technical monitor: Ken Zweibel

Department of Physics and Astronomy

The University of Toledo

Toledo, OH 43606

Summary

There are three focus area in this subcontract: cell structure and fabrication, cell modelling, and characterization of materials and devices.

Our efforts on cell fabrication have primarily involved the use of magnetron sputtering for deposition. In addition, we have developed and used novel electrochemical treatments at the stage of finishing the devices deposited by other techniques: vapor transfer deposition (VTD) and close space sublimation (CSS), both made at First Solar, LLC. During the second year of this award we have:

- made substrate CdS/CdTe solar cells using molybdenum foil, soda-lime glass, and SnO_2:F coated Tec 7 glass as substrates,

- developed ZnO:Al as front contact and ZnTe:N as a back contact to substrate cells,

- developed a technology of depositing Molybdenum on glass for substrate cells, including identification of stresses responsible for film failure and their mitigation,

- developed a series of new high-resistivity transparent (HRT) buffer layers that improve the device efficiency and allows for the use of thin CdS,

- established a new buffer layer effect: 'doping without dopants', which enables one to achieve high open-circuit voltages without the use of Cu,

- created a new class of electrolyte treatments that significantly change the device back contact, improve its uniformity, and can alone increase the cell efficiency from 3% to 11%,

- developed numerical modelling of current distribution in cells including nonuniformities in the main junction and back barrier,

- built a quantitative theory establishing figure of merit for nonuniformity effects in thin-film cells and predicted a phase transition between the regimes of weakly nonuniform and strongly nonuniform cells,

- devised biased-dependent photoluminescence mapping that allows for identification of major device flaws,

- studied properties of of ion-implanted Chlorine defects in CdTe crystals,

- for the first time identified the phenomenon of PL fatigue in thin-film photovoltaics and related it to the light-soak induced degradation,

- continued the defect-chemistry studies in collaboration with First Solar, LLC and found a stress dependent defect feature in PL spectra;

- created a new admittance spectroscopy "tool kit" that enables one to separate out the defect related features in the admittance spectra of CdTe devices,

- studied $CdCl_2$ treatment effects by means of X-ray absorption fine structure (XAFS),

- discovered the divergence in fluctuations of the main photovoltaic parameters under low light as a diagnostic tool for characterizing the device nonuniformity.

Much of this report covers work in progress and is therefore not fully complete. These efforts continue in Phase Three of This Contract.

Table of Contents

List of Figures

List of Tables

1. INTRODUCTION

1.1. Background

The purpose of this subcontract, as part of the R&D Partners Category of the Thin Film Photovoltaics Partnerships Program (TFPPP) of NREL is to 1) extend research efforts on cell structure and fabrication mainly through the use of magnetron sputtering, including absorber layer doping, window and back contact buffer layers, alternative back contacts, and preparation of inverted cell structures; 2) perform CdTe-based cell modeling which goes beyond traditional numerical models to include electric potential and electric current distributions in cells, the effects of nonuniformities in cell performance, and the physics of buffer layers; 3) to extend efforts on materials and device characterization with emphases on the use of photoluminescence (PL) including bias-dependent PL, as well as Hall effect and photo-Hall effect measurements, performed in parallel with current-voltage (I-V) and spectral quantum efficiency (SQE) device measurements; and 4) to support workforce development through the education and training of undergraduate, graduate, and postdoctoral students in the PV area.

This annual report covers the second year of a three year, NREL thin-film partnership subcontract with the University of Toledo which has three task areas: 1) cell structure and fabrication, 2) cell modeling, and 3) characterization of materials and devices.

1.2. Objectives of this subcontract

The primary objectives of this research by this subcontractor as an R&D partner is to address fundamental issues especially related to:

- enhancing the total-area, thin-film cell efficiency through magnetron sputtering of novel materials and alloys,

- improving the understanding of micro-nonuniformities and their impact on device and module performance through novel experiments and modeling,

- improving the understanding of the materials and devices through the use of photoluminescence (PL), capacitance-voltage (CV), Hall and photo-Hall, Raman, absorption,

1

and scanning electron microscopy (SEM) with energy dispersive x-ray spectroscopy (EDS),

- identifying materials and structural issues that can lead to improved cell stability, including interfacial layers and novel back contacts,

- identifying novel device structures to find pathways for reducing the utilization of CdTe, and development of substrate CdTe structures for comparison with standard superstrate devices and to determine possibilities for roll-to-roll manufacturing, and

- strengthening the thin-film PV infrastructure through education and training of undergraduate and graduate students as well as postdoctoral associates.

1.3. Technical approach

The scope of work under this subcontract is divided into three primary efforts which are reflected in the three following Sections. The first effort is focused on the use of magnetron sputtering for fabrication of CdTe-based cell structures. This includes the doping of CdTe during sputtering, the use of interfacial layers in sputtered cell structures, and the fabrication of (inverted structure) substrate cells on metal or metal-coated glass substrates. The second effort is focused on cell modeling. We seek to model quantitatively the effects of two-dimensional non-uniformities in electric potentials and current distributions in thin-film CdTe cells including the effects of buffer, absorber, and window layer parameters. The modeling effort includes comparison with cell and materials measurements, such as described in the third effort. The third effort is focused on the characterization of CdTe-based PV materials and devices. This effort includes studies of photoluminescence (PL) and electroluminescence (EL) of magnetron-sputtered (MS) and vapor-transport-deposited (VTD) materials and cells before and after stressing. The effort also includes small-spot PL (PL mapping) on standard cells and bias-dependent PL for direct comparison with the cell modeling efforts. We also have performed Hall, x-ray diffraction, Raman, SEM, capacitance-voltage, and synchrotron x-ray absorption studies on these materials.

2. CELL STRUCTURE AND FABRICATION

2.1. Sputtered Cells with T15/HRT substrates

Our earlier studies (reported in UT's 2002 Thin Film Partnership Program annual report) of using high resistivity transparent (HRT) buffer layers in sputtered CdS/CdTe cells showed results that were highly variable. We found that two different types of TEC15/HRT layers (# 609 and 691) gave very different results depending on whether the semiconductor deposition (CdS and CdTe) was done by CSS or by rf sputtering. Both of the HRTs (#609 and 691) gave poor results with sputtered CdS and CdTe but good results with VTD deposition. On the other hand, an earlier HRT (#C-24) gave excellent results with sputtering. Apparently the HRT deposition conditions and/or composition can affect the stability of the HRT in subsequent processing of the devices.

Therefore, during this Phase we studied a modified HRT layer (called "new HRT" in the text) on the TEC-15 substrates. Three different HRT resistivities were used for the fabrication of sputtered CdS/CdTe solar cells. The table 2.1 shows the electrical parameters of 1000 Å thick buffer layer used for sputtered solar cell fabrication, but determined from equivalent HRT depositions on glass.

Plate ID	Resistivity (Ω*cm)	Mobility (cm^2/V*s)	Carrier conc. (cm^{-3})
Y05-2	0.0295	6.98	3.0×10^{19}
Y14-5	0.123	5.74	9.0×10^{18}
Y11-5	0.269	4.12	6.0×10^{18}

Table 2.1: Electrical properties of HRT layer used for cell fabrication.

Since devices prepared by CSS deposition at high temperature ($> 550^oC$)on these new TEC15/HRT substrates showed good performance, we did a side-by-side comparison of sputtered cells using a half of the sputtered CdS plate was annealed in air at ∼550°C for ∼3 min before sputtered deposition of CdTe. A second half plate was completed without the high temperature anneal following the CdS deposition. Our earlier study with the (#C-24) HRT showed that the CdS thickness can be reduced to 80 nm in place of our standard 130 nm (used with TEC7 or TEC15 substrates without an HRT layer) to achieve high high J$_{sc}$,

reasonably good V_{oc} of ~800 mV and high efficiency of 13.5% (H923 in table 2.2). Therefore, we used 80 nm of CdS layer with these HRT substrates. Both halves of the TEC15/HRT/CdS plates (one annealed and one unannealed) were processed together for rest of the processing steps of CdTe deposition (80 nm) and CdCl$_2$ treatment. We also examined the effect of Cu diffusion on V_{oc}. The $V_{oc}$of all cells on each plate were measured, using a conducting foam probe, after the CdCl$_2$ treatments step but before Cu diffusion (called "V_{oc} without Cu"). Later the devices were completed using our standard Cu/Au back contact. Table 2.2 shows the detailed IV performance of the best cell on all the plates. For comparison, we prepared solar cells with standard CdS thickness (130 nm) both on TEC15/HRT (SSC110A2) and on the TEC15 without the HRT layer (SSC110B). Since one of the purposes of this study was to examine the compatibility of the HRT and CdS processing technique, cells were also fabricated with sputtered CdTe over the VTD CdS/HRT/TEC15 structure (SSC111B). The shapes of I-V curves of all solar cells were quite similar irrespective of HRT properties.

Sample ID	HRT layer	CdS thickness	CdS heat treatment	V_{oc} w/o Cu	V_{oc} with Cu	J_{sc}	FF	Eff.
SSC110B*	No	130 nm	No	730	814	20.41	69.78	11.59
SSC110A2	Yes	130 nm	No	795	799	19.4	63.2	9.79
SSC111B	Yes	70 nm	No, CSS CdS	760	814	23.07	57.34	10.77
T927A*	No	80 nm	No	580-600	722	22.23	68.12	10.93
H923**	Yes, C-24	80 nm	No	680-700	801	24.2	69.49	13.46
Y05-2A1	Yes	80 nm	No	750-795	819	20.54	60.75	10.22
Y05-2B2	Yes	80 nm	Yes	770-790	815	22.74	55.37	10.26
Y14-5B1	Yes	80 nm	No	780-795	804	19.61	66.31	10.45
Y14-5A2	Yes	80 nm	Yes	800-810	825	21.63	65.37	11.66
Y11-5A1	Yes	80 nm	No	725-775	799	20.92	66.79	11.17
Y11-5B1	Yes	80 nm	Yes	740-770	806	12.01	32.79	3.17

Table 2.2: Detailed I-V performance of devices on HRT substrate. * - Conducting substrate without HRT, ** - old HRT data. All other cells are on conducting TEC15/HRT substrate.

Before diffusion of Cu, the V_{oc} of cells on the new HRT was already high (typically 780 - 810 mV) and increased only marginally ($\sim$30 mV) after Cu diffusion. This is very different from cells on the old HRT (H923) or substrates without any HRT layer (SSC110B & T927A) where the initial V_{oc} was low (580-730 mV) which increased substantially (80-140 mV) after Cu diffusion, presumably due to an increase in carrier concentration in CdTe and improved electric field at CdS/CdTe junction. Once Cu is diffused during the back contact preparation, there is not much difference in the V_{oc} of cells with or without HRT layers.
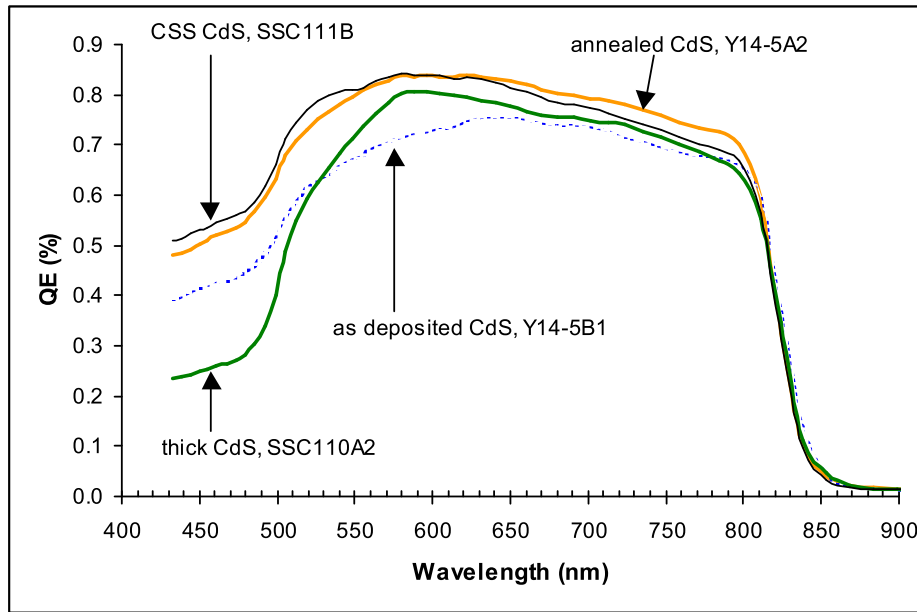
Figure 2.1: QE of few cells made on new HRT.

One of the purposes of using the HRT layer is to be able to reduce the CdS thickness and hence increase the J_{sc}. This effect is not observed in the new HRT (SSC110A2 and Y14-5B1 have similar J_{sc}) while the old HRT clearly demonstrated a high and increased J_{sc} of 24.2 mA/cm^2 (compare SSC110B and H923). The cells with annealed CdS showed an increase in J_{sc} ($\sim$10%) which is presumably due to improved crystallinity and transmission through the CdS. Figure 2.1 shows clearly the effect of CdS annealing (Y14-5B1 & Y14-5A2) on the QE of solar cells. The QE of the cell with annealed CdS improved not only in the blue region but throughout the entire visible spectrum which indicates better junction formation and current collection. The shape of the QE of Y14-5A2 is very similar to that of the cell made with thin CdS deposited using the CSS technique at $\sim$550°C (SSC111B9), which shows the

QE improvement, with these HRT substrates, of annealing after sputtering the CdS or of using a high temperature CdS deposition technique. Although the QEs are almost the same, the I-V measurement shows a higher J_{sc} for CSS deposited CdS cell. However, some cells with the sputtered and annealed CdS, although showing improved QE, often show a decrease in FF or V_{oc} so that the overall efficiency often shows little change. [For comparison, the QE of a cell (SSC110A2) with standard sputtered CdS (130 nm) thickness is also presented which shows a lower response in blue region in comparison with the QE of the thin CdS (80 nm) cell (Y14-5B1)].

Although an improvement of about 10% can sometimes be realized by annealing the sputtered CdS when this new HRT is used, in general, the devices prepared on this new HRT show similar efficiency, independent of whether the CdS is deposited by CSS or sputtering. Therefore the new HRT seems quite compatible with the sputtering process. (This is unlike the HRT layers (#609 and #691) that were examined in the previous Phase, which showed poor results for sputtered CdS and CdTe.) Also, cells show relatively little difference in cell efficiency due to annealing of CdS. However, there is some evidence of variability when this new HRT layer is used. The J_{sc} and FF value of cells with annealed CdS (Y11-5B1) is very poor which is due to some visible interdiffusion/reaction or damage occurred during annealing.

Even though we were able to achieve high V_{oc} and good efficiency using HRT substrates, the glass side reflection of these solar cells were non-uniform green/blue in most of the cases which is quite different from the cells prepared on conducting glass without HRT layer. This could be due to chemical reaction/interdiffusion at the HRT/CdS interface, and may be a reason for poor yield on these substrates.

2.2. Substrate solar cells

In this section we report on the fabrication of substrate CdS/CdTe solar cells. In such structures, the p-n junction is more accessible to measurements, being unshielded by glass and finished later in the process cycle. Our substrate cells also have no copper. Copper can have both beneficial and detrimental effects on solar cells; copper is believed to stabilize cell performance, but it also is a fast diffuser along grain boundaries and can lead to shunting. Copper-free cells can serve as a control to understand the effects of copper.
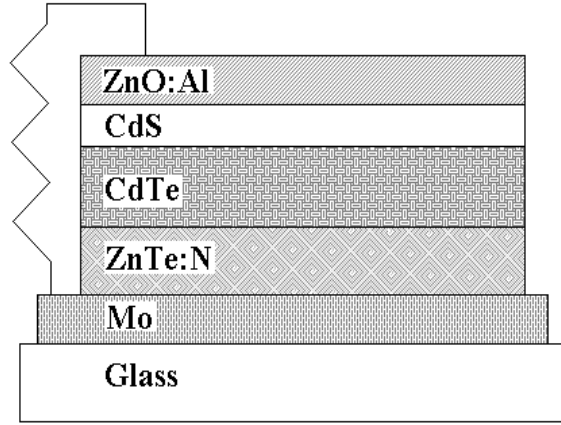
Figure 2.2: Substrate Solar Cell Structure. Built on soda lime or Tec 7 glass; the terminals are the molybdenum back contact and ZnO:Al front contact. Substrate cells on molybdenum foil (not shown) have an additional undoped ZnTe layer between ZnTe:N and CdTe.

Cells were built using molybdenum foil, soda-lime glass, and SnO_2:F coated Tec-7 glass as substrates. The Mo on the glass was dc sputtered. These multiple substrates were used to aid understanding of the sputtered Mo layer. Cells built on molybdenum foil are identified with a number ID (such as Mo-40), while cells built on glass (either Tec-7 or soda lime glass) are identified with a letter ID (e.g., Mo-ah). The general structure is as shown in Figure 2.2. We have made two inverted structures on Mo foil with 3% N_2 in the sputter gas. One of these structures was made with thicker ZnTe:N. Deposited film thicknesses are shown in Table 2.3.

Cell ID	Substrate material	ZnTe:N (μm)	ZnTe (μm)	CdTe (μm)	CdS (μm)
Mo-40	Moly foil	0.07	0.03	2.4	0.16
Mo-41	Moly foil	0.17	0.03	2.4	0.16
Moah	Glass slides	0.2	0	2.4	0.16
Moai	Tec 7	0.2	0	2.4	0.16

Table 2.3: Thickness of layers for substrate cells.

The opacity of the molybdenum prevents in situ determination of the thickness of the semiconductor layers with optical absorption. The growth rates for the materials were determined individually, using optical absorption when possible or (in the case of Mo) by

7

scribing films and measuring the depth of the scribe with a stylus profilometer. The thickness of the layers in the final devices was then estimated by the growth rate and deposition time. Sputtered molybdenum on glass was in all cases estimated to be 0.6 μm thick.

The ZnTe:N on Mo-ah and Mo-ai was annealed 45 minutes at 200°C in air before the deposition of CdTe/CdS. In all cases, the ZnTe:N was etched with a 0.3 % by volume dilute mixture of HCl and de-ionized water before the deposition of the CdTe/CdS layers. All cells were CdCl$_2$ treated prior to the deposition of ZnO:Al contacts, by RF sputtering through a mask with 0.079 cm^2 holes.

Cell ID	V_{oc} (mV)	J_{sc} (mA/cm^2)	Fill Factor (%)	R-Series (Ohm cm^2)	R-Shunt (kOhm cm^2)	Efficiency (%)
Mo40-69	678	21.0	44.6	18.96	0.196	6.4
Mo41-18	366	4.1	31.0	62.57	0.136	0.4
Moah-53	540	7.9	29.3	93.42	0.139	1.3
Moai-16	625	27.3	33.5	25.74	0.069	5.7

Table 2.4: Best contact data.
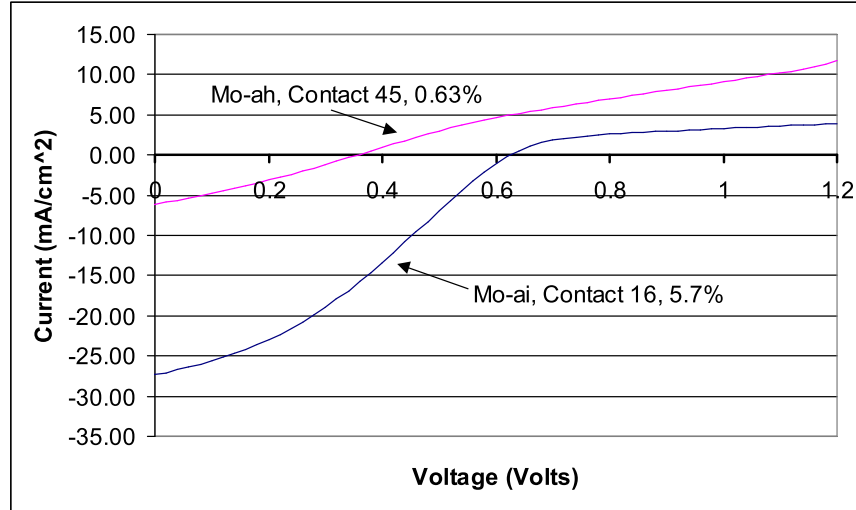
Figure 2.3: Substrate Cells' IV.

All plates had some shorted cells with Mo-41 showing the lowest performance overall. The other plates were improved by decreasing the thickness of the ZnTe:N/ZnTe layer.

Most contacts have roll-over in the current-voltage curve, indicating problems at the back junction. The best contacts data are presented in Table 2.4.

The current-voltage curve is shown in Figure 2.3. The Mo-ai contact 16 is the best cell from that plate; however, its IV curve shows features representative of many substrate cells' IV. Notable is the roll-over past open circuit voltage, the slope near short circuit, and the low fill factor. While typical, the extreme roll-over is not always present in substrate cells, but its presence does not correlate to anything obvious (substrate - Mo foil or glass - or cell performance). IV from another contact is included to show less severe roll-over in substrate cells.
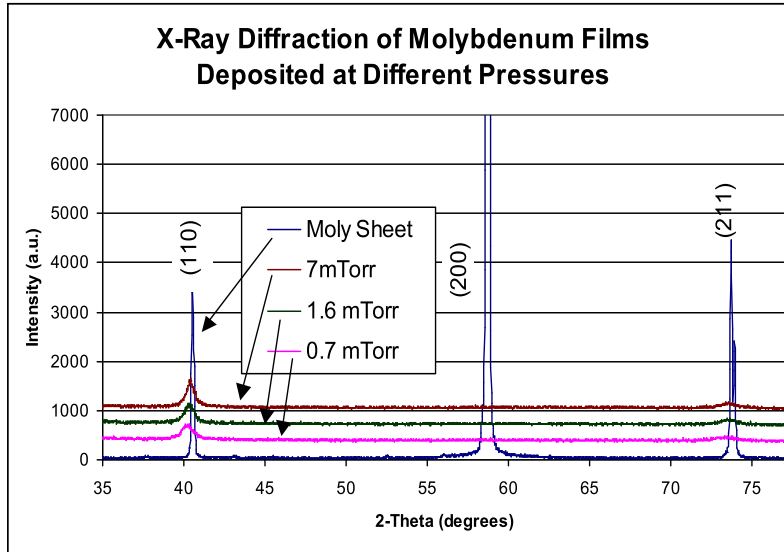
Figure 2.4: X-Ray diffraction of sputtered films of different deposition pressures and for (lowest trace) Mo foil. Curves are shifted vertically for clarity.

2.3. Stress in Molybdenum Films

The first depositions of molybdenum on glass for substrate solar cells resulted in the molybdenum cracking and delaminating due to compressive strain. This problem was solved by increasing the deposition pressure. Stress arises in thin films from a variety of sources. We believe the dominant source of compressive stress in our films was atomic peening: the collision of high energy sputtered atoms against the film. At higher pressures, there are more

gas molecules for sputtered atoms to collide with, which reduces the energy of sputtered atoms before they reach the target and in turn lessens the effect of atomic peening. The effects of stress in our films at different deposition pressures were studied in more detail with x-ray diffraction. Figure 2.4 shows XRD data of three molybdenum films deposited at different pressures, as well as that of a molybdenum sheet. The molybdenum sheet shows strong (110), (200), and (211) peaks. The films show a noticeable (110) peak, but only a weak (211) peak and no (200) peak. The weakness of the higher order peaks is partly due to the low film thickness but there also appears little (200) oriented grains in the sputtered film.

Sample	$< 110 >$ Separation (Angstroms)
Reference	3.1468
Molybdenum Sheet	3.1469 +/- 0.0007
7 mTorr Deposited	3.156 +/- 0.003
1.6 mTorr Deposited	3.162 +/- 0.002
0.7 mTorr Deposited	3.17 +/- 0.01

Table 2.5: Shift in Lattice Constant with Deposition Pressure.

The (110) peak is also seen to shift to lower values of 2-Theta at lower deposition pressures (see Figure 2.5 and Table 2.5), corresponding to increasing planar separation. The planar separation is measured along the scattering vector; that is, perpendicular to the film. Compressive stress in the plane of the film will produce the observed elongation in the perpendicular direction.

Shift in (110) XRD Peak for Different Deposition Pressures
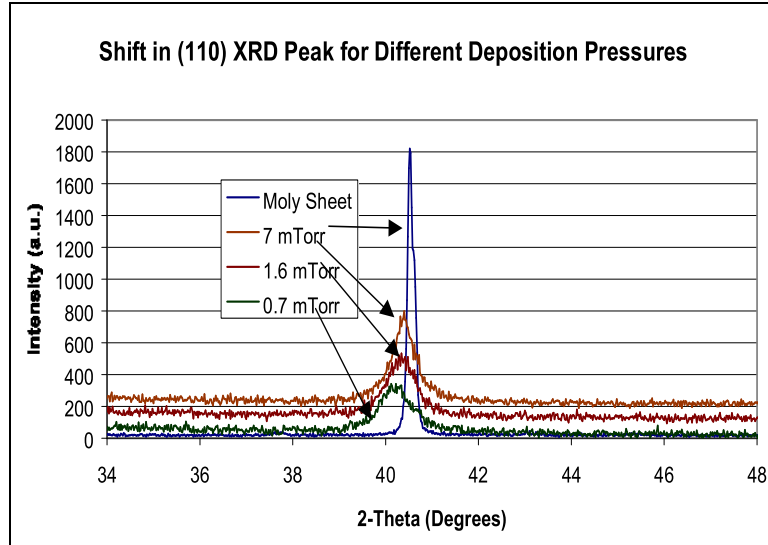
Figure 2.5: Shift in $< 110 >$ XRD Peak for different deposition pressures. The $< 110 >$ peak in sputtered molybdenum films is seen to shift to lower values of 2-Theta with lower deposition pressures.

3. CELL MODELING

3.1. Numerical modeling of current distribution and comparison with thermography measurements

In recent years, lateral nonuniformity has become an important issue, in particular because of the urgent need to scale small laboratory-prepared devices up to large commercially-manufactured modules. Significant variations in photovoltaic parameters between nominally identical devices is one practically important consequence of nonuniformity. Since individual cells in a module are interconnected, occasional bad parts affect the whole device performance and stability. The nonuniformity appears on different scales as detected by different mapping techniques, such as surface photovoltage, optical beam and electron-beam-induced current, recombination lifetime, photoluminescence, etc. (see 1,2 and references therein).

Lock-in thermography has proven a valuable technique for nonuniformity diagnostics in crystalline and multi-crystalline solar cells.[3,4] It utilizes the ac IR imaging of a device, where the temperature is affected by an external ac voltage of the same (lock-in) frequency. The thermography maps thus represent the current distributions. Surprisingly, this technique remained relatively new to thin-film technology, where non-uniformity effects are most detrimental. Here we present for the first time the IR lock-in thermography data and corresponding modeling for polycrystalline thin-film CdTe/CdS solar cells. The thermography measurements were done in collaboration with J.P. Rakotoniaina and O. Breitenstein of Max-Planck-Institut für Mikrostrukturphysik in Halle, Germany.

For this study, devices were prepared by three different deposition techniques: radio-frequency sputtering, vapor transport deposition (VTD), and close spaced sublimation. In all cases, a layer of CdS followed by a CdTe layer was deposited on commercially available SnO_2-coated glass substrate. The latter transparent conductive oxide (TCO) served as a front electrode. After deposition, the samples were submitted to a standard anneal in the presence of $CdCl_2$ vapor, which generally leads to improved electrical characteristics. Finally, a metal layer was deposited to form the back contact to CdTe. Devices were measured as prepared and then after 56 days of light soak stress, conducted at open circuit under 1 sun illumination, 65^oC . Such stress is often used to study the device efficiency degradation.

The lock-in thermography was carried out using the commercial TDL 384 M 'Lock-in'

thermography system by Thermosensorik GmbH (Erlangen).[5] Several samples of each lot have been measured at a lock-in frequency of 3 Hz in two modes: a) forward bias pulses (0 to 0.8 - 1 V) under laboratory light condition (nominally, in the dark), b) forward bias pulses (0 to 0.8 - 1 V) under continuous illumination. Different forward biases were used in order to have comparable forward currents of about 3 mA/cm^2, leading to comparable thermographic signals. Cells were imaged from the back contact side, since the substrate was not transparent to the IR light of 3-5 μm used. The sample was contacted with a pin with a small piece of nickel foil placed below to avoid scratching. Since the metallized area had a low IR emissivity, the phase image, which is independent of the IR emissivity, was also regarded. In some cases the IR emissivity was increased by covering the surface with a black paint.

Shown in Fig. 3.6 are amplitude images scaled up to a maximum temperature modulation amplitude of 3 mK (the contacting probe is visible in the lower right corner of each map). Figs. 3.6a and 3.6b show the typical maps obtained in the dark and under illumination respectively. Generally, we observed much lower thermal signal in the dark. While this particular device was prepared by the VTD technique, we did not see significant differences in the observed features between this and other cells. In most cases the edge of the cell showed a larger thermal signal (bright contour line), even after covering the cell with a black paint; the phase signal indicated the same.

Fig. 3.6(c) shows the same cell measured under illumination after light soak stress. The thermography signal intensity typically increased by a factor of ~ 3 after the stress, becoming more nonuniform. This map also shows one very bright spot, which we identify as a non-ohmic shunt, not visible under reverse bias. Some of the cells developed true shunts in the process of light-induced degradation. The bright edge line width increased after the light soak.

Summarizing, several typical features are identifiable: (1) considerable signal inhomogeneity, increasing after light soak stress (consistent with the result in Ref. 6), and pointing to lateral inhomogeneities in the current flow, (2) bright contour line corresponding to higher signal at the cell edge, (3) rare spots of very high signal, in most cases not visible under reverse bias and (4) dark area off the contact.

We attribute the above features to spatial variations in the device local characteristics. This is reflected in the model of random diodes connected in parallel through a resistive
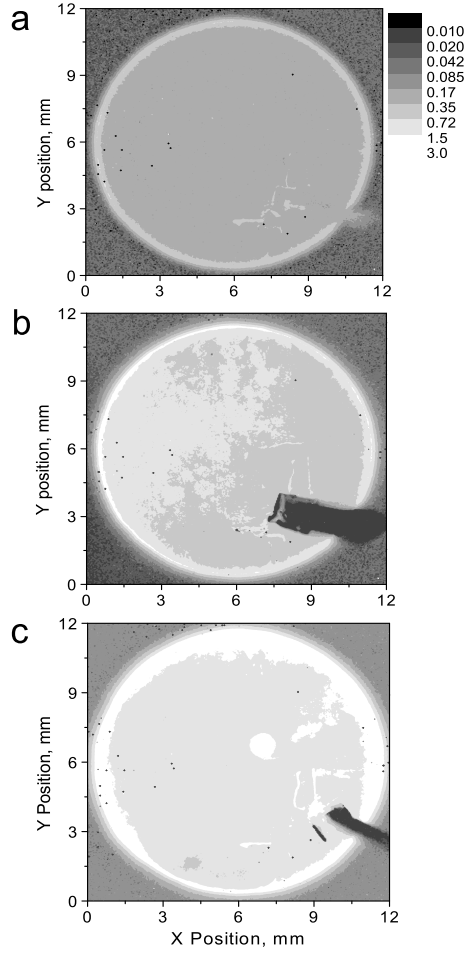
Figure 3.6: Typical thermography maps obtained for a CdTe/CdS solar cell measured a) in dark, b) under illumination and c) under illumination after light soak stress.

electrode,[1,2] as illustrated in Fig. 3.7 (see also 7,8 for multi-crystalline Si solar cells). Series resistors qualitatively represent the back barrier (back diode) effect, attributed to the CdTe-metal interface.[10,11] The back barrier is suppressed beyond the contact.

We used the equivalent circuit in Fig. 3.7 for numerical simulations with the following input parameters: open-circuit voltage V_{oc} , series resistance R_s, shunt resistance R_{sh} on each diode, and sheet resistance of the most resistive layer R_r (TCO for metallized area, or semiconductor sheet resistance for a contact-free area), bias voltage V applied at the edge of a cell as a boundary condition. Given the latter parameters and the non-ideality factor, the standard diode equation[12] was used to calculate the current in each of the units.

To simulate a nonuniform system, the individual diode parameters, V_{oc}, R_s, etc., were
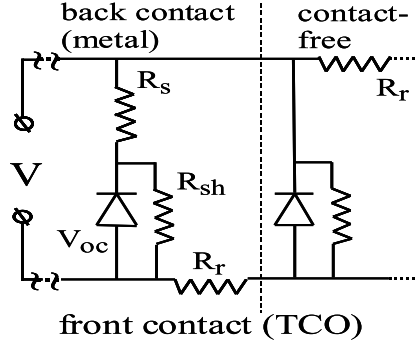
Figure 3.7: Equivalent circuit for the numerical simulation program. For simplicity we show a one-dimensional case. Note, R_r is different for metallized and contact-free areas as explained in the text.

randomly generated to obey either Gaussian or uniform distributions with the typically observed[1,2] respective averages and dispersions. The electric potential and current distributions in the circuit were then calculated by numerically solving a set of Kirchhoff's equations.

For this study we simulated a two-dimensional system of 30 by 30 diodes. The input parameters were chosen to correctly predict the typically observed current-voltage characteristics. The effects of disorder were modelled by the uniform V_{oc} distribution with relative mean-square-root fluctuation of 10%, and the Gaussian R_s distribution with relative standard deviation of 25%. The Gaussian distribution for R_s was chosen to allow for rare spots of negligibly small R_s that mimic the back barrier pinholes.

We have chosen the parameter distribution corresponding to two contacts separated by a contact-free area. The resulting map of currents is shown in Fig. 3.8a. Similar to the thermography maps, the current distribution in contacts is inhomogeneous. We also observe a bright line corresponding to high current value near contact edges followed by a dark region of zero current from contact-free area. Physically, the bright edge feature is due to the higher forward current density through a narrow region bordering with the contact. This region provides a low-resistance pathway where the back barrier is absent and R_s=0. A bright spot in the upper contact represents an abnormally weak diode with V_{oc} three times lower than the average value. Shown in Figs. 3.8 b,c are two other features predicted by our modeling: a pinhole in the back barrier ($R_s = 0$) and a combination of the pinhole with a weak (low V_{oc}) diode. The latter serves as a strong shunt that robs current from a large surrounding
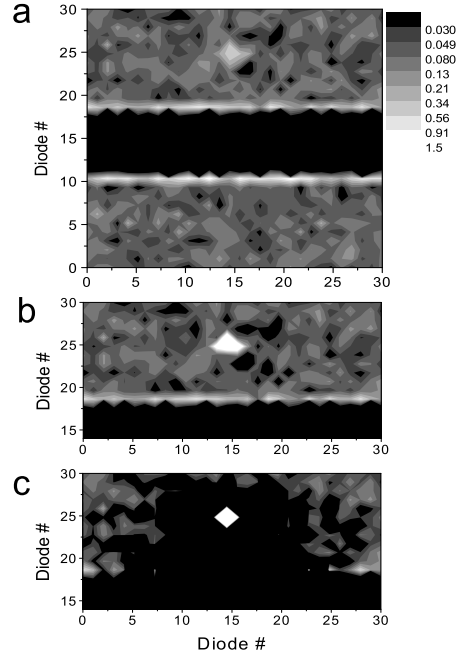
Figure 3.8: a) Map of currents (relative units) obtained from numerical simulations with random V_{oc} and R_s. Shown is an area with two contacts and contact-free region between them. The upper contact shows one bright spot corresponding to low V_{oc}. b) The upper half of the map with the bright spot now corresponding to $R_s=0$ (back barrier pinhole). c) The result of combining low V_{oc} and $R_s=0$ at the same spot.

area.

To further explain the bright edge feature, we note that the current decay beyond the metallized region occurs in the form of branching similar to the well-known dc transmission line.[9] Based on the latter analogy one can estimate the current decay length as $l = \sqrt{R_\perp / R_\parallel}$, where $1/R_\perp$ is the transversal conductance per unit length and $R_\parallel$ is the resistance per unit length in the lateral direction. For a round cell of radius r these two quantities can be expressed as $R_\perp = R_{oc}(\pi r^2/b)$ and $R_\parallel = \rho_s/b$. Here R_{oc} is the cell open circuit resistance, b is the device thickness, ρ_s is the semiconductor sheet resistance. This yields

$$l = r\sqrt{\pi R_{oc}/\rho_s}. \tag{3.1}$$

We identify l with the bright line width. Substituting into Eq. (3.1) the typical values $R_{oc} \sim 3\Omega$ and $\rho_s \sim 10^4 \Omega/\square$ for CdTe under ambient illumination, we estimate $l \simeq 0.3$ mm,

consistent with our measurements (Figs. 3.6 a,b). Since R_{oc} typically increases after the light soak stress, Eq. (3.1) also offers an explanation for the observed increase in the bright ring width after the degradation (Fig. 3.6c).

In conclusion, we present the lock-in thermography data and related random-diode model simulation for CdTe/CdS solar cells. We identify the main observed features and show that all of them can be simulated in the framework of our model. Our results demonstrate that IR lock-in thermography is a valuable technique for thin film solar cell diagnostic, revealing non-uniformities in the device back contact and main junction. One more specific result of this study is that the degree of non-uniformity correlates with the device deterioration usually observed under light soak stress.

3.2. Towards quantitative theory of laterally nonuniform photovoltaics

This Section treats large area noncrystalline photovoltaics as a new class of disordered systems, random diode arrays (RDA). The physics of such devices is strongly determined by the material inhomogeneity and the presence of potential barriers in p-n and other junctions[12]. Correspondingly, a prototype RDA is a set of random photo-diodes connected in parallel through a resistive electrode. Other possible applications of RDA beyond photovoltaics include charge transport across monomolecular layers where an organic molecule can act as a diode[13], electrically coupled light emitters[14], stochastic heterostructures in nanotubes[15], and spin-polarized electron transport through a domain wall[16].

Each diode in RDA has the ideal current-voltage $(j - V)$ characteristic

$$j = j_0\{\exp[e(V - V_{oc})/kT] - 1\}, \tag{3.2}$$

where kT and e have their standard meaning, j_0 and V_{oc} are local diode parameters. The open-circuit voltage (V_{oc}) fluctuations have exponentially strong effect on RDA currents and are considered the main nonuniformity source. A simple nonrestrictive example is a bimodal V_{oc} distribution representing identical weak (low V_{oc}) diodes imbedded in the uniform matrix of more robust units. Both one-dimensional (1D) and 2D systems are of practical interest.

From the theoretical standpoint, the problem is to describe the topography and statistics of random electric potential in RDA and predict its integral characteristics. This nonlinear problem requires approaches beyond the standard theory of disordered systems. One such

approach is developed below for the case of infinitely large RDA with uncorrelated disorder.

Qualitative analysis. A nontrivial part of the problem is that micro-diodes interact with each other by forcing currents through a resistive electrode. On intuitive grounds, the interaction is characterized by the correlation length

$$L_0 = \sqrt{kT/e\rho j_0}. \tag{3.3}$$

Its physical meaning is that the characteristic thermal fluctuation in the electric potential $\delta V = kT/e$ is balanced by the potential drop $j_0 L_0^2 \rho$ across the electrode of linear dimension L_0. For D=1, $L_0 \rho$ and $j_0 L_0$ represent the resistance and current, and ρ is the resistance per unit length. For D=2, ρ is the sheet resistance and the current is $j_0 L_0^2$. For stronger fluctuations $\delta V > kT/e$ the correlation length is even larger, $L = L_0 \sqrt{e|\delta V|/kT} > L_0$. L_0 and L vary over a wide range depending on the system parameters and can be macroscopically large (see the numerical estimates below).

We assume in what follows that the characteristic diode size in RDA is small, $l \ll L$ (see numerical estimates below) and thus a large number $(L/l)^D \gg 1$ of random diodes contribute to RDA characteristics. Consider, for simplicity, a bimodal V_{oc} distribution with low weak diode concentration, $(l/R)^D \ll 1$ where R is the average nearest weak diode distance. The average RDA potential is determined by the condition that the sum of all currents given by Eq. (3.2) vanishes,

$$\overline{V} = -(kT/e) \ln\langle \exp(-eV_{oc}/kT) \rangle. \tag{3.4}$$

Weak diodes find themselves under forward bias $\overline{V} - V_{oc} > 0$ and exponentially large positive currents. Strong diodes ($\overline{V} - V_{oc} < 0$) run negative currents $\approx j_0$. Eq. (3.4) states that weak diodes have exponentially strong effect.

The relative dispersion ξ_D in the bare weak micro-diode currents turns out to be a significant parameter characterizing the system nonuniformity. It can be estimated by noting that each weak diode consumes exponentially strong relative current $\exp[e(\overline{V} - V_{oc})/kT]$ and that in the region of linear size L_0 the relative fluctuation in the weak diode number is $\delta N/N \sim 1/\sqrt{N} \sim (R/L_0)^{D/2}$. This gives

$$\xi_D \sim (R/L_0)^D \exp[2e(\overline{V} - V_{oc})/kT]. \tag{3.5}$$

One can expect that the disorder effects are significant when $\xi_D \gg 1$; this prediction is verified below.

Parameter estimates. Practically required transparent electrodes in RDA related devices cannot be made of a 'good' metal; hence, substantial sheet resistance $\rho \sim 10\Omega/\square$[17]. The current density is $j_0 \sim (1-3) \cdot 10^{-2}\text{A/cm}^2$ (under one sun illumination) for most photovoltaics[17]. For the room temperature, this yields $L_0 \sim 1$ mm, however L_0 is by the factor of 100 larger under the ambient room light (lower j_0). Hence, random diodes interact across macroscopic distances. Note that such length scales comparable to the device element sizes may cause mesoscopic effects. For the main fluctuating parameter V_{oc} it is typical to have $\langle eV_{oc}/kT \rangle \sim 10-30$ with the characteristic relative fluctuation of $\sim 0.1-0.3$ (see[1,2] and references therein). The weak diode distance R is not well known and based on different mapping techniques can be in the range of tens to hundreds of microns[1]. Substituting this into Eq. (3.5) shows that both the cases of strong ($\xi \gg 1$) and weak ($\xi \ll 1$) disorder are realistic.

Quantitative approach. The electric potential distribution in RDA can be described based on the diode equation (3.2) and the Ohm's law:

$$\nabla \mathbf{i} = -j, \quad \rho \mathbf{i} = -\nabla V, \tag{3.6}$$

where $\mathbf{i}$ is the lateral current (current density) in the resistive electrode for D=1 (D=2), V is the electric potential, and j_0 is the specific transversal currents (per length for D=1 or per area for D=2) defined in Eq. (3.2). Introducing the dimensionless units

$$\phi = e(V - \overline{V})/kT, \quad y = x/L_0, \tag{3.7}$$

equations (3.6) can be reduced to the form

$$\nabla^2 \phi = (1 + \zeta) \exp(\phi) - 1 \tag{3.8}$$

where ζ is a random variable,

$$\zeta = \exp[e(\overline{V} - V_{oc})/kT] - 1, \quad \langle \zeta \rangle = 0. \tag{3.9}$$

Its statistics is described by the correlation function

$$\langle \zeta(0)\zeta(\mathbf{r}) \rangle = B\delta(\mathbf{r}), \quad B = const. \tag{3.10}$$

Here $\delta(\mathbf{r})$ is the delta-function of the coordinate $\mathbf{r}$. [Because of the micro-diode finite size, $\delta(\mathbf{r})$ should be understood as having a small yet finite width l].

In what follows ϕ is presented as a superposition of the short-range and long-range components,

$$\phi = \phi_s + \phi_L, \quad |\phi_s| \ll 1, \quad \langle \phi_s \rangle = 0. \tag{3.11}$$

ϕ_s has the characteristic space scale $l \ll 1$. Its amplitude is assumed to be small, $\varphi_s \ll 1$, since the neighboring micro-diodes are separated by small electrical resistance; the corresponding condition is derived in Eq. (3.20) below. The long-range component is not necessarily small and is approximately constant on the scale of l.

Linearizing Eq. (3.8) in $|\phi_s| \ll 1$ and averaging over a region of linear dimension x, such that $l \ll x \ll 1$, yields

$$\nabla^2 \phi_L = (1 + \langle \phi_s \zeta \rangle_x) \exp(\phi_L) - 1. \tag{3.12}$$

In accordance with the central limit theorem, a random quantity $\langle \phi_s \zeta \rangle_x$ should obey the Gaussian statistics. Its fluctuations are relatively small, since the averaging is taken over a large number of microdiodes $(x/l)^D \gg 1$.

Eliminating the terms absorbed by Eq. (3.12) and neglecting ϕ_s in its right-hand-side, linearized Eq. (3.8) becomes

$$\nabla^2 \phi_s = \zeta \exp(\phi_L), \tag{3.13}$$

where ϕ_L is considered constant. A system of coupled equations (3.12) and (3.13) describe the long-range and short-range components of the electric potential.

The quantity $\langle \phi_s \zeta \rangle_x$ in Eq. (3.12) can be expressed through the correlation function $\langle \zeta(0)\phi_s(r) \rangle$ with $r = l$. Multiplying Eq. (3.13) by $\zeta(0)$ and then averaging gives the equation

$$\nabla^2 \langle \zeta(0)\phi_s \rangle_x = B\delta(\mathbf{r}) \exp(\phi_L), \tag{3.14}$$

whose particular solution is

$$\langle \zeta(0)\phi_s \rangle_x = \exp(\phi_L) \begin{cases} B|r|/2 & \text{for} \quad D = 1, \\ (B/2\pi) \ln r & \text{for} \quad D = 2. \end{cases} \tag{3.15}$$

Constants that may appear in its general solution must be determined from the boundary conditions. Because Eq. (3.13) is restricted to the region $r \ll 1$, the standard boundary condition is hard to impose. Offering an alternative is the observation that, in the absence of other characteristic lengths, the correlation between ζ and ϕ_s should decay over distances $r \sim 1$. The required decay automatically follows from Eq. (3.15) for the case of D=2. For

D=1, a negative constant needs to be added to the solution in Eq. (3.15) to ensure the decay. [The latter analysis of $\langle \zeta(0)\phi_s \rangle$ can be easily verified for the case of a small disorder where Eq. (3.8) becomes linear in ϕ.] Substituting into Eq. (3.15) $r = l$ and adding $-BL/2$ for the case of D=1, yields

$$\nabla^2 \phi_L = -\frac{1}{4\xi}\left[\exp(\phi_L + \ln 2\xi) - 1\right]^2 + \frac{1}{4\xi} - 1, \tag{3.16}$$

where

$$\xi = \frac{B}{2} \cdot \begin{cases} 1 & \text{for} \quad D = 1, \\ (1/\pi)\ln(1/l) & \text{for} \quad D = 2. \end{cases} \tag{3.17}$$

While aimed at describing RDA, Eq. (3.16) does not contain random variables. As explained below, the factors accounting for the disorder are different for the cases of small and large ξ.

One immediate result of the above analysis is that there exists a critical disorder, $\xi_c = 1/4$, such that the electric potential and current distributions are qualitatively different for the cases of $\xi < \xi_c$ and $\xi > \xi_c$. In the case of subcritical disorder $\xi < \xi_c$ one can calculate the average potential in the system by setting the left-hand-side zero in Eq. (3.16),

$$\langle \phi_L \rangle = \ln\left(\frac{1 - \sqrt{1 - 4\xi}}{2\xi}\right). \tag{3.18}$$

This solution fails when $\xi > 1/4$. Furthermore, analyzing the corrections $\delta\phi_L \equiv \phi - \langle\phi\rangle$ by perturbation technique, it is straightforward to see from Eq. (3.16) that the characteristic length scale and amplitude of nonuniformities diverge as ξ approaches $\xi_c = 1/4$. Hence, ξ is a figure of merit for the nonuniformity effects. Estimating B as defined in Eq. (3.10) for a bimodal V_{oc} distribution and substituting it into Eq. (3.17) leads to $\xi \sim \xi_D$. Therefore, ξ represents the relative dispersion in the bare weak diode currents. Below we consider the cases of subcritical and supercritical disorder separately.

Subcritical disorder. $\langle \zeta(0)\phi_s \rangle_x$ was calculated in the above through the correlation function $\langle \zeta(0)\zeta(\mathbf{r}) \rangle$ defined for the infinite system in Eq. (3.10). As pointed after Eq. (3.12), the finite size effects make B a Gaussian random quantity with the relative standard deviation of the order of $(l/x)^{D/2} \sim l^{D/2} \ll 1$. The corresponding variations $\delta\xi$ become an important source of randomness for small $\xi \ll 1$ when the r.h.s. in Eq. (3.16) is dominated by the contribution that is inversely proportional to ξ. Because $\delta\xi$s are small, so are the variations in ϕ_L (the system is almost uniform). They satisfy the linearized equation (3.16),

$$\nabla^2 \delta\phi_L = \langle\phi\rangle\sqrt{1 - 4\xi}\delta\phi_L - \delta\xi \exp\langle 2\phi\rangle \tag{3.19}$$

21
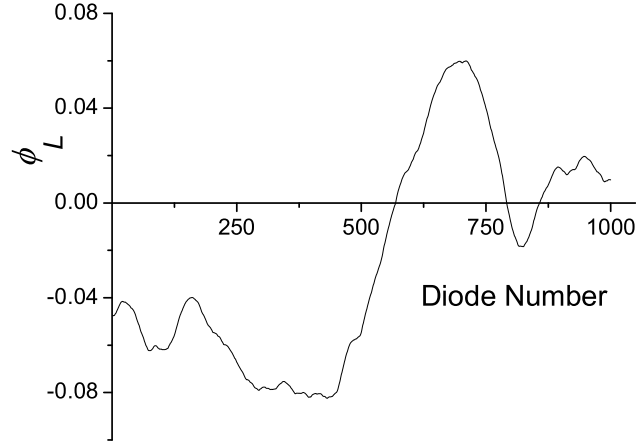
Figure 3.9: 1D ϕ_L distribution for the case of subcritical disorder numerically simulated for a random diode circuit with uniformly distributed V_{oc}. The diode number plays the role of the linear coordinate. Note small amplitude of the fluctuations.

and thus obey the Gaussian statistics.

Supercritical disorder. For $\xi > \xi_c$, the r.h.s. of Eq. (3.16) is everywhere negative. The negative curvature $\nabla^2\phi$ exponentially increases in the absolute value with ϕ above its maximum $\phi_m = \ln(1/2\xi)$. Therefore, the spectrum of ϕ cannot span much beyond ϕ_m. Indeed, any increase in ϕ (i. e. positive $\nabla\phi$) would be strongly limited by exponentially large negative $\nabla^2\phi$. For $\xi \gg \xi_c$ and $\phi < \phi_m$ we find $\nabla^2\phi \approx -1$ that is $\phi(\mathbf{r})$ is close to a negative curvature paraboloid and is unbounded below. This is consistent with the above observation that the average $\langle\phi\rangle$ is not defined when $\xi > \xi_c$.

The unbounded spectrum appears in the framework of the approximation employed. The lower boundary effects can be included beyond that approximation by accounting for the lowest ϕ's that correspond to the weakest diodes. In the above approximation framework, the weakest diode appears a singularity where $\nabla\phi$ undergoes a finite change and the electric potential cannot be decomposed into a sum of long- and short-range components. Taking such singularities into account, the potential has a piecewise continuous structure formed by a set of negative curvature paraboloids (far from weak diodes where the approximation of smoothly varying potential is valid), connected in a singular way at weak diodes (see Figs. 3.10, 3.11).

The location of singularities need to be further specified if the V_{oc} distribution is not a
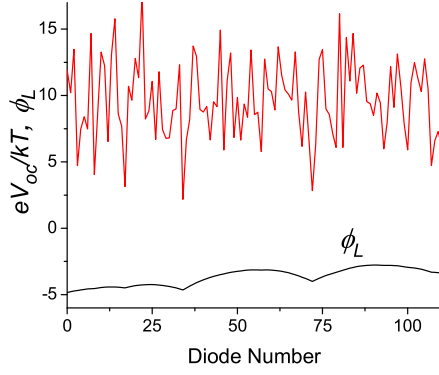
Figure 3.10: V_{oc} and reduced electric potential ϕ distributions for the case of supercritical disorder numerically simulated for a 1D random diode circuit. Note singular ϕ shapes in the proximity of minima.

bimodal. A diode weakest in its screening length neighborhood ($V_{oc} = V_{oc,\min}$) will obviously cause a singularity. On physical grounds, a less weak diode at distance r in the same neighborhood will cause a singularity if it is a local current sink. This happens when the difference between its V_{oc} and $V_{oc,\min}$ is smaller than the electric potential drop $j_0\rho r^2$ across the resistive electrode between the two diodes. This understanding is consistent with the results of numerical modelling (Figs. 3.10, 3.11).

Applicability. The linearization of Eq. (3.8) with respect to ϕ_s remains valid when $\langle\phi_s^2\rangle \ll 1$. Multiplying Eq. (3.13) by $\phi_s(0)$, averaging, and taking into account Eqs. (3.15) and (3.17), reduces the latter condition to

$$\langle\phi_s^2\rangle = \xi\exp(2\phi_L) \ll 1. \tag{3.20}$$

It is obviously satisfied for the case of subcritical disorder, $\xi \ll 1$. For $\xi \gg 1$, we take into account that the spectrum of ϕ_L is confined to the region $\phi_L \lesssim \ln(1/2\xi)$. As substituted in Eq. (3.20) this gives $\langle\phi_s^2\rangle \lesssim 1/4\xi \ll 1$; hence, the inequality in Eq. (3.20) obeys in the far supercritical region. However it fails in the critical region.

Numerical simulations. As a verification, 1D and 2D RDAs of 1000 diodes have been simulated numerically. The individual diode V_{oc}s were randomly generated to obey either Gaussian or uniform distributions with desired averages and dispersions. The electric potential and current distributions were then found by numerically solving a set of Kirchhoff's equations with the open circuit boundary conditions.
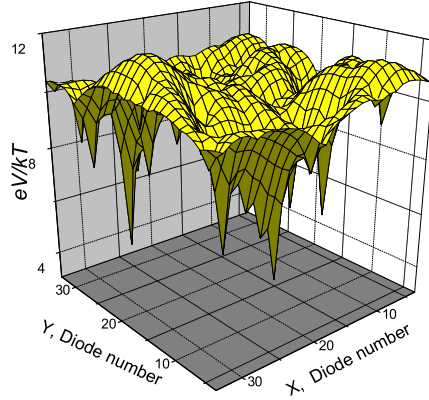
Figure 3.11: Electric potential distribution for the case of 2D supercritical disorder numerically simulated for RDA of 31x31 diodes. Note cusps in the proximity of minima and paraboloidal shapes far from them.

For RDA with subcritical disorder the distribution in Fig. 3.9 has a smoothly varying shape similar to what is typically considered random potential in the existing theory of disordered systems. Such shape, smallness of the potential fluctuations, and their verified Gaussian statistics are consistent with the above analytical predictions.

The results of numerical simulations for 1D and 2D RDA with supercritical disorder are shown in Figs. 3.10 and 3.11. They confirm, indeed, the conclusion of piecewise continuous potential distribution of randomly located negative curvature paraboloids forming cusps in connection points.

Example implication. As an implication of the above theory consider the tail of the probabilistic distribution of weak diode currents (i. e. $j > 0$) in RDA. A weak diode current is stronger when it does not have equal competitors in a larger domain and thus robs currents generated by a larger number of neighboring robust diodes. The probability of finding no weak diodes in the region of large radius $r > R$ is given by the Poisson distribution $\exp[-(r/R)^D]$. Because the amplitude of electric potential $\delta\phi$ is parabolic in r, we get $\delta\phi \propto r^2$. The electric current can be expressed as $J \sim \delta\phi/(\rho r^{(2-D)})$ where $D = 1, 2$ [see the discussion after Eq. (3.3)]. As a result the probability distribution for the current takes the form

$$g(J) \propto \exp(-J/J_0) \quad \text{for} \quad J > J_0, \tag{3.21}$$

24

for both the cases of D=1 and D=2 where $J_0 = j_0 R^D = const$ (in conventional units). This prediction agrees well with the results of numerical simulations.

To conclude, RDA represent a new class of nonlinear disordered systems modeling large area semiconductor devices. They are predicted to undergo a phase transition from the state of almost uniform to that of strongly nonuniform electric potential; the corresponding order parameter (figure of merit, ξ) and its critical value are derived. From the practical standpoint, this understanding can serve as a guide for technology to mitigate the nonuniformity effects. The established piecewise continuous topography of random potential represents a new concept in the physics of thin-film photovoltaics. The above consideration leaves unanswered many important questions. Those of the role of the boundary conditions for finite RDA, their $j - V$ characteristics, mesoscopic effects, and properties of RDA of other topologies seem to be the most challenging.

The major practical result is that the apparent device uniformity can be a consequence of subcritical fluctuation regime and does not necessary guarantee the absence of nonuniformity loss in a device.

3.3. Buffer and interfacial layer effects

3.3.1. Known effects of buffer layer

To improve the efficiency of CdS/CdTe cells a thinner CdS layer is often used, which increases the number of photons reaching the CdTe layer. However, making CdS thinner can lead to pinholes through which CdTe physically contacts the TCO layer thus shorting the device. In order to prevent this mechanism, a highly resistive transparent (HRT) buffer layer is deposited between the TCO and CdS. In general, it is possible to distinguish between two major effects of the buffer layer, namely its effects on pinholes and on the p-n junction, as discussed below.

Effect on pinholes Buffer layer can put resistive 'clogs' on pinholes thus minimizing their detrimental effects. This action can be efficient for small diameter pinholes, since the 'clog' resistance is inversely proportional to the pinhole crossectional area $\pi d^2/4$. More specifically, the 'clog' resistance needs to be greater than the TCO sheet resistance in order to block the

pinhole. This results in the condition

$$\rho_{HRT} > \frac{\pi d^2}{4l^2} \rho_{TCO}, \qquad (3.22)$$

where ρ_{HRT} and ρ_{TCO} are the sheet resistances of HRT and TCO respectively, and l is the HRT thickness. Given the parameters in Table 3.6, this transforms into the inequality

$$d < (10 \div 100)l \qquad (3.23)$$

where the multiplier in the parenthesis depends on the particular buffer layer parameters. Assuming as a rough estimate $l \sim 0.1$ μm, the latter criterion becomes $d < 1 \div 10$ μm. This is definitely larger than the CdS grain size (~ 0.1 μm); hence the buffer layers used in this study would block the pinholes of tens and even hundreds missing CdS grains. It however could not be helpful in blocking the larger scale pinholes that are sometime visible in the device by the naked eye. At this point we conclude that the buffer layers used in our study are useful in blocking not very large pinholes in the devices.

Whether the pinhole action dominates its useful properties or there are other buffer layer actions, can be verified by studying the buffer layer effects in devices with different CdS thicknesses. If the buffer layer only action were to prevent pinholes, then, as the thickness of the CdS layer increases, the number of pinholes should decrease and there should be no difference between a sample with and without buffer layer. This is not what we have observed in the present study. We shall see in what follows that the presence of buffer layer strongly affects even the devices with thick CdS layers.

Effect on the junction It is believed the main junction in a CdS/CdTe device occurs between the n-type CdS layer and the p-type CdTe layer. The depletion widths of both semiconductors are given by:

$$x_1 = \left[\frac{2N_{A2}\epsilon_1\epsilon_2 \left(V_{bi} - V\right)}{qN_{D1} \left(\epsilon_1 N_{D1} + \epsilon_2 N_{A2}\right)} \right]^{1/2} \quad \text{and} \quad x_2 = \left[\frac{2N_{D1}\epsilon_1\epsilon_2 \left(V_{bi} - V\right)}{qN_{A2} \left(\epsilon_1 N_{D1} + \epsilon_2 N_{A2}\right)} \right]^{1/2},$$

where N_{A2} is the hole concentration of CdTe, N_{D1} is the electron concentration of CdS, V_{bi} is the built-in voltage and the other values have their usual meanings.

The hole concentration in CdTe is estimated to be around 10^{14} holes/cm^3, and the electron concentration in CdS to be around 10^{17} electrons/cm^3 (see for example [18]). If we consider a built-in voltage of 0.8V, $\epsilon_2 = 10\epsilon_0$, $\epsilon_1 = 6\epsilon_0$,$V = 0$, and the carrier concentrations in CdTe of 10^{14} and of 10^{17} cm^{-3} in CdS, then we obtain:

$x_1 \approx 3 \ \mu$m and $x_2 \approx 30$ Å

In follows then that the screening length in CdS is rather short. In particular, any sample which has a CdS thickness greater than a few hundred A will screen possible buffer layer effect on the main junction. In other words, from the point of view of the standard junction theory, the presence of the buffer layer should not affect the main junction parameters of our devices. We will see in what follows that the latter prediction is inconsistent with the observed buffer layer effect that have been found to propogate through even thick CdS layers.

Buffer	Thickness (Å)	Sheet resistance ($\Omega/\square$)	Resistivity (Ω*cm)	Hall mobility (cm^2/V*s)	Carrier concentration (cm^{-3})
	600	$2.1\text{x}10^3$	$1.26\text{x}10^{-2}$	5.1	$9.7\text{x}10^{19}$
A	1000	$8.0\text{x}10^2$	$8.04\text{x}10^{-3}$	6.9	$1.1\text{x}10^{20}$
	2000	$3.6\text{x}10^2$	$7.24\text{x}10^{-3}$	6.9	$1.2\text{x}10^{20}$
	600	$2.9\text{x}10^3$	$1.74\text{x}10^{-2}$	7.9	$4.5\text{x}10^{19}$
B	1000	$2.9\text{x}10^3$	$2.95\text{x}10^{-2}$	7.0	$3.0\text{x}10^{19}$
	2000	$1.3\text{x}10^3$	$2.65\text{x}10^{-2}$	7.4	$3.2\text{x}10^{19}$
	600	$9.4\text{x}10^3$	$5.67\text{x}10^{-2}$	6.8	$1.6\text{x}10^{19}$
C	1000	$1.2\text{x}10^4$	$1.23\text{x}10^{-1}$	5.7	$8.8\text{x}10^{18}$
	2000	$1.1\text{x}10^4$	$2.25\text{x}10^{-1}$	2.6	$1.1\text{x}10^{19}$
	600	$2.8\text{x}10^4$	$1.68\text{x}10^{-1}$	5.5	$6.8\text{x}10^{18}$
D	1000	$2.7\text{x}10^4$	$2.67\text{x}10^{-1}$	4.1	$5.8\text{x}10^{18}$
	2000	$2.6\text{x}10^4$	$5.00\text{x}10^{-1}$	3.4	$3.6\text{x}10^{18}$
	600	$2.3\text{x}10^5$	1.41	2.6	$1.8\text{x}10^{18}$
E	1000	$2.1\text{x}10^5$	2.11	2.5	$1.4\text{x}10^{18}$
	2000	$6.8\text{x}10^5$	13.6	2.5	$1.8\text{x}10^{17}$

Table 3.6: Electrical properties of the buffer layer films.

Electronic properties of the buffer layer   In our study, buffer layers were deposited on Tec15 from Pilkington using several conditions and different thicknesses. Their electrical properties were monitored by Hall measurement (Table 3.6) by depositing a film of the same condition on non-coated glass.
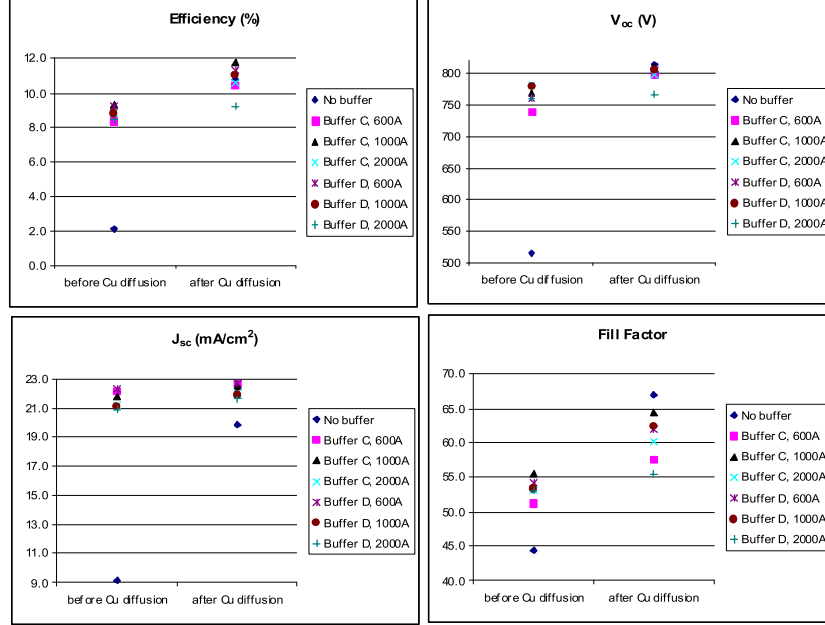
Figure 3.12: J-V results for cells with buffer layer.

CdS and CdTe were deposited on TEC15 and on conditions C and E by Close Space Sublimation (CSS) at First Solar, LLC. The CdS thickness was around 800 Å for the samples with a buffer layer, and 3000 Å for the sample without any buffer layer. The CdTe thickness was around 3.5 μm. The cells undergo the standard $CdCl_2$ treatment which is known to improve the efficiency of the devices, and then a thin layer of Cu was deposited on the films. Current-voltage (J-V) (fig 3.1), quantum efficiency (QE) (fig 3.2) and capacitance-voltage (C-V) (fig 3.3) characteristics were taken before and after heat treatment to diffuse the Cu into the CdTe film, after deposition of the metal back contact. The J-V results showed are an average of 10 cells of 1.1 cm^2 area. QE and CV measurement were taken on only 1 cell, on the same spot on the different cells. QE measurements were taken at 3 different bias, -1V, 0V and +0.4V. The C-V measurements were taken at 75 kHz.

Buffer layer effects on the device J-V and QE characteristics   In our experiments buffer layer has shown remarkably strong effects before Cu diffusion and much weaker effects on the device with Cu fully diffused (see Figs. 3.12, 3.13, 3.14 and 3.15). We can summarize our results as follows.

- Before Cu diffusion

28
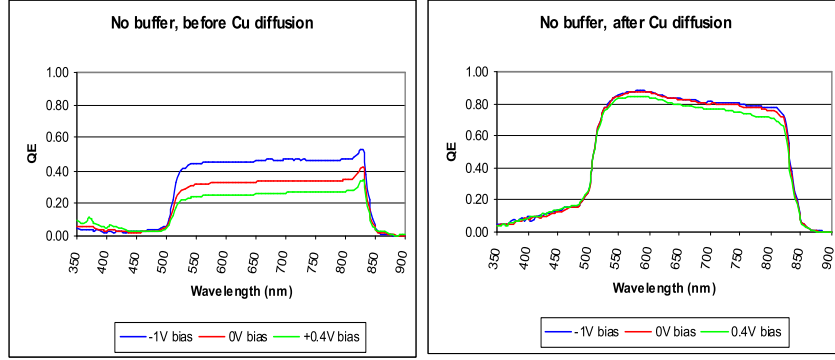
Figure 3.13: QE results without buffer.

- V_{oc}s of samples with buffer layer are close to 800 mV, as opposed to the samples without any buffer (V_{oc}s around 500 mV). This phenomenon was noticed for several samples without any buffer layer. In our opinion, the high V_{oc}s observed for the buffer containing samples mean than, a good junction is formed in the presence of buffer layer even before Cu. As is seen in Fig. 3.12, this is observed for both thin and thick CdS-layer samples and is in clear contradiction with what was anticipated in the above based on the standard theory of the electron screening in CdS.

- J_{sc}s are already high before Cu diffusion in the buffer layer containing samples, which again means that there i sa well developed junction where good carrier collection takes place. This is confirmed by the QE measurements in Fig. 3.14. Furthermore, for the samples containing a buffer layer, only a slight improvement in carrier collection is reached under the bias of -1V, again, testifying in favor of good junction, as oppose dto the data for the no-buffer samples before Cu diffusion shown in Fig. 3.13.

- The fill factor is poor before Cu diffusion and is not improved by the buffer layer. This can be explained by the back contact barrier series resistance that need Cu diffusion to be improved.

- After Cu diffusion

  - After Cu diffusion no significant differences are observed in device efficiencies between the samples without any buffer layer and those with the buffer layer, the

29
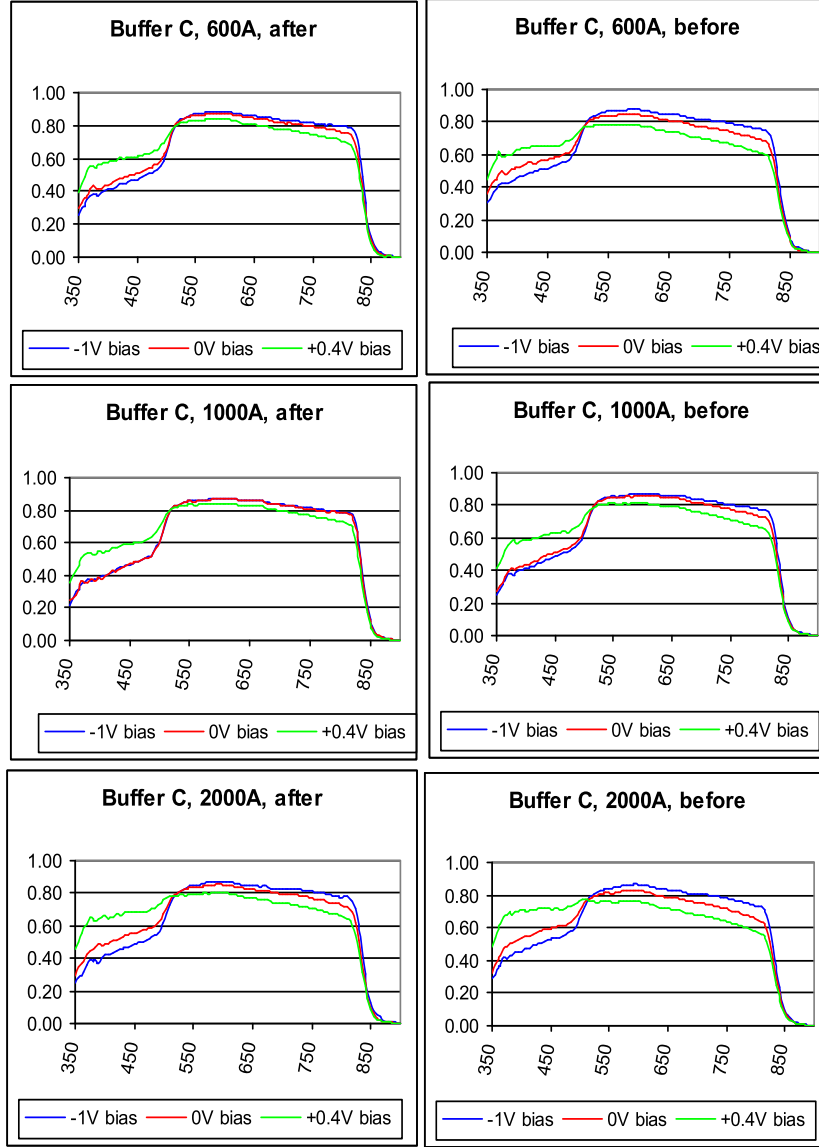
Figure 3.14: QE results for buffer condition C, different buffer thickness, before and after Cu diffusion.

only exception being the most resistive buffer layer.

– V_{oc}s achieved the same value around 800 mV.

– Slight improvement in current for the samples containing a buffer layer, which is due to a slightly better carrier collection of the CdTe in the red (see QE), whereas the sample without any buffer shows a huge change in QE (see Figs. 3.13, 3.14 and 3.15).
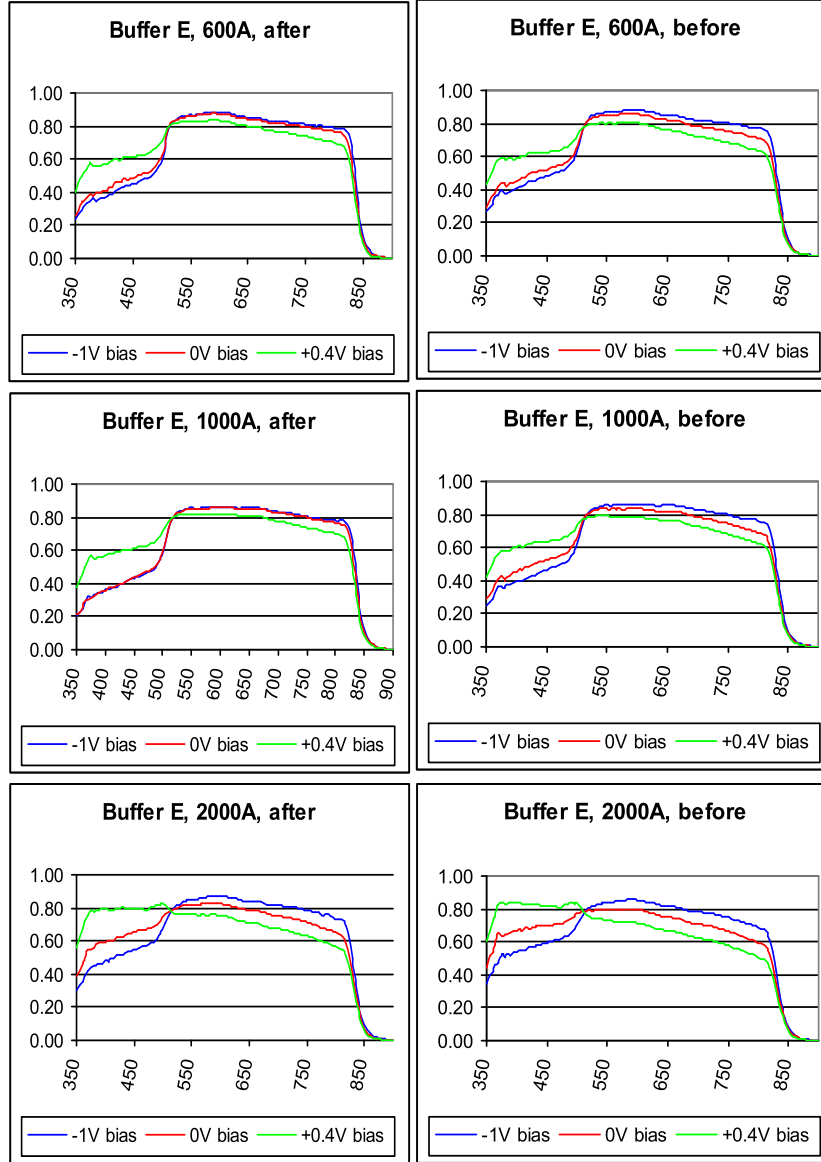
Figure 3.15: QE results for buffer condition E, different buffer thickness, before and after Cu diffusion.

C-V results

- For the sample without any buffer layer, the C-V dependance is flat before Cu diffusion. That points at the standard geometrical capacitance, supposedly between the TCO and the metal back contact. After Cu diffusion, the $1/C^2$ vs. V curve shows a standard response typical of good p-n junctions (Fig. 3.16).

- The samples with a buffer layer before Cu diffusion show C-V curves similar to that
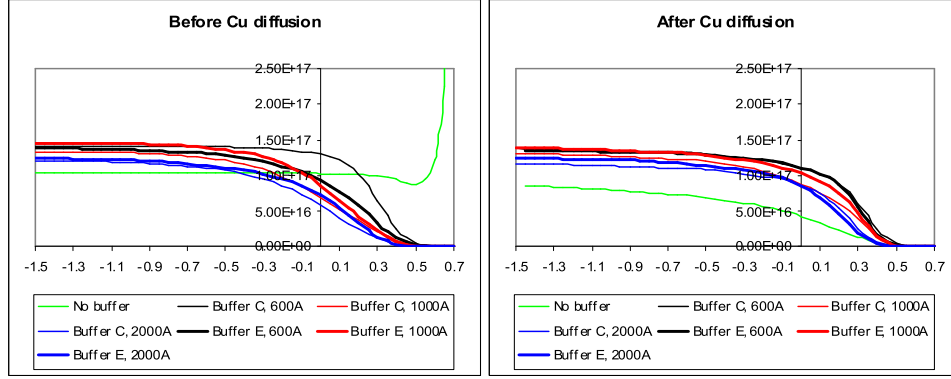
Figure 3.16: Capacitance ($1/C^2$ vs. V) results for two buffer conditions (C and E) and different buffer layer thickness before and after Cu diffusion.

of Cu-diffused ones. Under reverse bias, between -1.5V to -1V, before and after Cu diffusion the curves are quite flat, which could mean that the carrier concentration in CdTe is approximately constant. The most noticeable part is the steep slope of the curves is in between -0.5V and 0.5V.

Cell stability studies For device stability experiments, 1000 Å thick buffer layer of condition C was chosen as it seems to give the best performance. A buffer layer between the TCO and the CdS is supposed to improve the stability of the device as it could prevent diffusion of species from the TCO to the CdS and vice-versa. One other concern for the devices stability is the influence of copper. Because samples with buffer layer have already good efficiencies before Cu diffusion, the following samples and schedules were used:

- Tec15, CSS CdS (~ 1000Å and ~ 3000Å), CSS CdTe (~ 3.5 μm), Cu

- Tec15, buffer, CSS CdS (~ 1000Å), CSS CdTe (~ 3.5 μm), no Cu, with and without heat treatment

- Tec15, buffer, CSS CdS (~ 1000Å), CSS CdTe (~ 3.5 μm), Cu, with and without heat treatment

Ten 1.1cm^2 cells were finished on each of the plates and J-V readings taken after post-metal deposition treatment, and then after 1 day, 4 days and 7 days of light soak at 65°C under 1 sun light intensity.
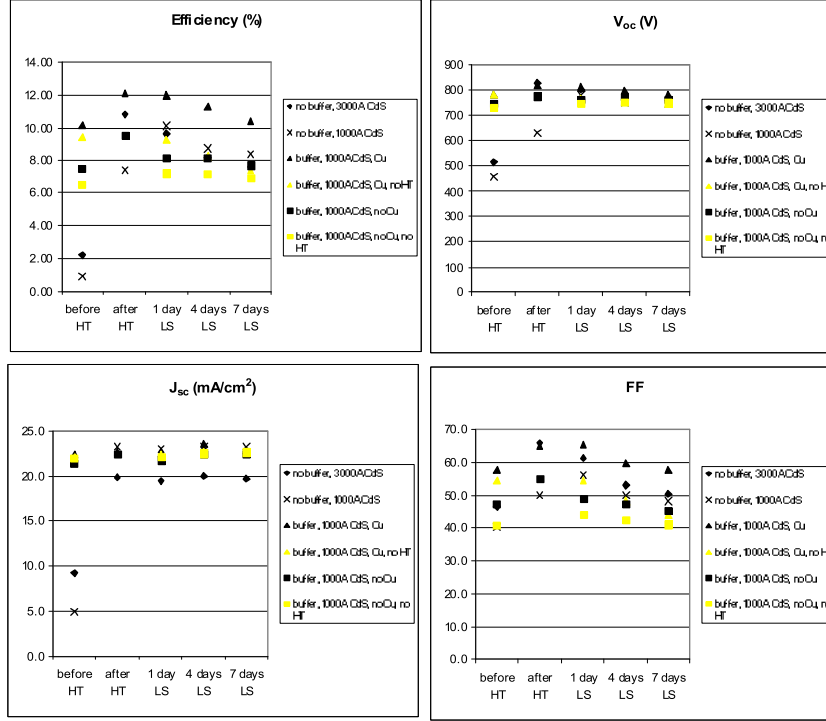
Figure 3.17: J-V parameters stability results.

Again, good efficiencies were achieved for the cells with buffer layer, as opposed to the cells without buffer layer before heat treatment. The buffer layer does not seem to increase the stability of the device. Only a sample with buffer layer and no Cu doping seems to be more stable over time. Longer light soak studies are necessary to confirm the latter tendency.

Summary of buffer layer effects The above J-V, QE and C-V measurement data unambiguously point at the fact that buffer layers have direct profound effect on the device main junction. More specifically, these data show that the main junction of good quality is formed in the presence of buffer layer even without additional Cu doping. To the contrary, in the absence of buffer layer, Cu-doping is needed to create a decent quality main junction.

We can also conclude that buffer layer helps to block pinholes of not very large diameters ($\lesssim 10 \ \mu$m), while its effects on the larger pinholes are less significant.

So far our observations did not show any effect of buffer layers on the device degradation and stability. Longer time light soak studies are necessary to verify the latter observation.

Of the major significance is the observation that buffer layer extends its effect through a relatively thick CdS layer (thickness much greater than the screening length). This implies

33

a new physical mechanism of thin-film junction formation. The corresponding work is now in progress and will be described in our final report.

3.3.2. Electrolyte treatment

With active area requirements of up to one square meter, CdTe devices cannot be made crystalline and are polycrystalline. Associated with their noncrystallinity are lateral device nonuniformities over micron length scales, that include variations in grain size, chemical composition, etc. The structural fluctuation effects are aggravated by barrier-controlled transport that is exponentially sensitive to the barrier parameters related to the device junctions and grain boundaries. In fact, considerable lateral nonuniformities have been observed in all major thin-film PV by different mappings and in the form of variations between nominally identical devices (see Refs. 1,2 and references therein). They have also been indicated in multi-crystalline silicon solar cells.[19]

Understanding of lateral fluctuations lies in the device diode nature and in the electrode resistivity that is substantial for optically transparent electrodes. Hence, an equivalent circuit of random micro-diodes connected in parallel through a resistive electrode represents a thin-film PV cell.[1,2] In the ideal-diode approximation, each microdiode current-voltage (j-V) characteristic is

$$j = j_0\{\exp[e(V - V_{oc})/kT] - 1\}, \tag{3.24}$$

where kT and e have their standard meaning. The open-circuit voltage V_{oc} fluctuations have exponentially strong effects, and seem to be the major source of nonuniformity.

Weak (low V_{oc}) microdiodes are most detrimental to the device, since they find themselves under forward bias generated by their more robust neighbors. As a result they a) rob currents, thereby decreasing the device generated power, and b) localize stresses and thus promote nonuniform degradation.[1,2,20] Based on this understanding, blocking weak diodes seems to be a straightforward way of improving the device performance and stability. A non-trivial part of the problem dealt with in this Letter is to devise a treatment that selectively blocks the weak diodes while keeping the rest of the device intact.[21]

Our approach is illustrated in Fig. 3.18 where the surface photovoltage varies across a semiconductor film exposed to light and immersed in an electrolyte. The surface potential variations in the electrolyte bring about currents that (in accordance with the Le Chatelier's
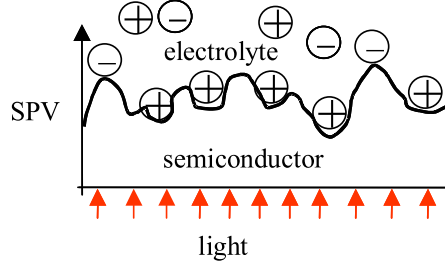
Figure 3.18: Sketch of the experimental setup of selective electrochemical treatment. The fluctuating surface photovoltage (SPV) corresponds to the CdTe surface of CdS/CdTe polycrystalline device

principle) tend to reduce the variations. In a properly chosen electrolyte, this may result in selective etching and/or depositing local surface 'clogs' at the weak diode spots where the electric potential is a minimum. If these surface modifications are electrically insulating or otherwise active (electric double layer, etc.), then the weak diodes will be blocked (passivated) and will not affect the device performance after subsequent metal deposition. We call such a process self-healing to reflect the fact that it selectively acts on the weakest spots of the device.

The above process can also be described in the terms of an interfacial layer (IFL) deposited on a semiconductor thin film to level out its lateral nonuniformity. Indeed, it was recently shown[20] that a properly selected IFL can cause such an effect in a commercially available thin-film CdTe devices, although the mechanisms behind the IFL action remained a puzzle.

Theoretical Analysis. Two factors were taken into account in designing a proper electrolyte treatment. The first one is to use the fluctuations of V_{oc} to drive electrochemical reactions that selectively target weak spots.

The second factor is the electrolyte resistivity r. On physical grounds, the smaller the value of r, the larger is the characteristic length L_e, across which electrically different spots in the film surface interact through the electrolyte [cf. Eq. (3.26) below]. To ensure that the treatment effectively levels out the nonuniformities, L_e needs to be greater than the characteristic nonuniformity length in a completed device under working conditions.

To further specify the latter criterion one should discriminate between the micro-structure

nonuniformity length l and the length L of the electric nonuniformity induced by variations in local micro-diode parameters. Typically, l varies in the range of microns to hundreds of microns.[1,2,19] L is determined by the presence of an electrode, through which a micrononuniformity extends its influence across significant distances (say, $L \sim 1$ cm) as explained next. Since $L \gg l$, the above criterion becomes $L_e > L$.

The length L can be expressed as[1]

$$L = \sqrt{|u|/\rho j_0}. \tag{3.25}$$

The physical meaning of L is that the electric potential fluctuation u is balanced by the potential drop $j_0 L^2 \rho$ across the resistive electrode of linear dimension L. Here ρ is the sheet resistance and the current is $j_0 L^2$. The maximum $L_{\max}$ corresponds to a dead shunt ($u = V_{oc}$). The minimum L_0 is defined by Eq. (3.25) with $u = kT/e$. Given the typical PV parameters, $j_0 \sim 20$ mA/cm^2, $\rho \sim 10\Omega/\square$, and room temperature $kT/e \sim 0.025$ V, $L_0 \sim 3$ mm under 1 sun illumination.

The electrolyte screening length L_e can be derived along the same lines. We take into account that the electric potential drop balancing the nonuniformity u occurs across the effective three-dimensional resistor of the characteristic size L_e, whose resistance is $\sim r/L$. This yields

$$L_e = |u|/r j_0. \tag{3.26}$$

For a numerical estimate we consider an electrolyte whose resistivity $r \sim 10$ $\Omega\cdot$cm, of the order of that of 1 Molar aqueous NaCl solution. Substituting also, $kT/e \sim 0.025$ V and $j_0 \sim 20$ mA/cm^2 yields $L_e \sim 1$ mm. The required inequality $L < L_e$ can also be presented in the form

$$r < \rho L j_{0s}/j_{0e} \tag{3.27}$$

where j_{0s} and j_{0e} are the currents j_0 corresponding to the light intensities under the device working condition and the electrolytic treatment, respectively. With typical $\rho \sim 10\Omega/\square$ and $L \sim 1$ cm this results in $r \lesssim 10$ $\Omega\cdot$cm. The inequality in Eq. (3.27) remains valid for higher r in combination with lower j_{0e}. Based on Faraday's law, such lower j_{0e} will deposit equally massive layer over longer time period $\propto 1/j_{0e}$.

Experimental results. The typical experimental device consists of a 0.15 μm layer of CdS followed by a 3.5 - 4 μm CdTe layer deposited on commercially available SnO$_2$-coated glass
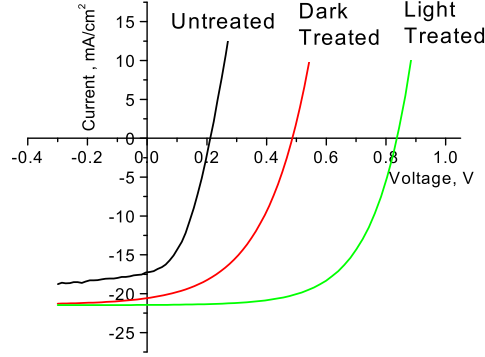
Figure 3.19: Effect of electrolyte surface treatments and 1 hour 1 sun light exposure on the CdS/CdTe I-V curves

substrates. The conductive oxide layer of a sheet resistance $\rho = 15\Omega/\square$ served as the front electrode. The semiconductor layers were created by the vapor transport deposition, after which the samples were submitted to the standard anneal in the presence of $CdCl_2$, which generally leads to improved electrical characteristics.[22] After the anneal, the typical grain sizes for CdTe were about 1-2 μm. Cu was introduced at the metal-semiconductor junction through the anneal step. This is believed to also lead to the formation of a strongly doped p-layer at the CdTe surface helping in the formation of a good back contact.[23,24] After the electrolyte treatment (if any) a metal layer was sputtered to form the back contact to CdTe.

For the electrolyte treatments we used a mixture of 0.2M aniline, 0.01M p-toluenesulfonic acid and NaCl in deionized water. [Aniline was chosen for its ability to electropolymerize in acidic media at low potential[25], comparable to surface photovoltage fluctuations]. The solution resistivity was in the range from 1 to 200 Ω·cm depending on the NaCl content. The light of intensity 0.01 to 1 sun was coming through the glass side of an uncompleted device (before the back contact deposition). The electrolyte was applied at room temperature onto the CdTe side of the structure shown in Fig. 3.18. The tungsten-halogen lamp light used in our experiments was completely absorbed in CdTe and thus did not interact with the electrolyte. Correspondingly, any difference between the results of 'light' and 'dark' treatments were attributed to the light-induced effect in the device and not in the electrolyte. A change in the color of CdTe surface to a lighter gray was noticed after successful treatments.

Shown in Fig. 3.19 results indicate, indeed, a strong positive effect of the electrolyte treatments applied under the light, as opposed to the dark electrolyte treatments. In many
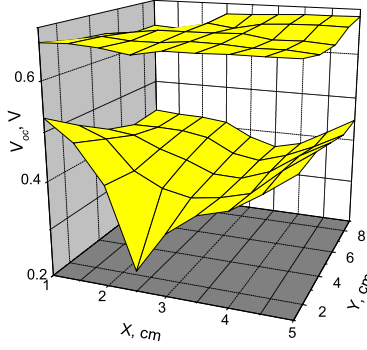
Figure 3.20: Open circuit electric potential variations of CdS/CdTe device with intentionally high resistive back contact (5 nm Chrome) under low light of 0.01 sun for the electrolyte treated and untreated cases.

cases it improved the solar cell efficiency from, say, 2% to more than 11%.

We verified that decreasing the light intensity from 1 to 0.1 sun and simultaneously increasing the exposure time by the factor of 10 led to similar improvements in the device parameters. However, over such a long period of time, the acid present in the solution, might cause an etching effect thereby modifying CdTe surface.

To further verify the possibility of etching we used aniline free mixtures. Again, a considerable improvement of the light (but not the dark) treated samples was observed, even though the degree of improvement was not as significant as that for the aniline containing solution. More experimenting is needed to understand the chemical nature of the aniline effect. Two plausible mechanisms are 'clogging' weak diodes and voids (that would otherwise evolve into shunts as metallized), and forming a layer that protects the etched surface from oxidation before the metal is deposited.

We have also observed that after a given exposure time the treatment lost its efficiency as the resistivity increased. However, simultaneously decreasing the light intensity to the level that keeps the product rj_{0e} intact, and increasing the exposure time $\propto 1/j_{0e}$ restored the treatment effect. This observation is fully consistent with our theoretical understanding and the criterion in Eq. (3.27). We were able to quantitatively verify the latter criterion by using the parameters of our devices and the measured solution resistivity.

Finally we have verified a considerable change in the degree of nonuniformity between the light and dark treated samples by mapping the V_{oc} distribution in 10x5 cm^2 samples with

deposited thin (5 nm) chrome layer, whose sheet resistance (~ 1 kΩ) is high enough to keep the local areas at a distance of $L \sim 1$ mm electrically insulated (under 1 sun illumination). As shown in Fig. 3.20, the treated samples are indeed more uniform and have higher V_{oc}. Remarkably, the surface photovoltage in the light and dark treated devices was the same before the metal deposition. This is consistent with our understanding of weak micro-diodes as a primary nonuniformity source that extend their influence through the electrode.

In conclusion, we have put forward the concept of photovoltaic self-healing that selectively blocks the effects of lateral nonuniformities in thin-film semiconductor structures. We have quantitatively described the required parameters of the underlying electrolyte treatment and devised a specific chemical composition of such a treatment for CdTe/CdS photovoltaic devices. A dramatic improvement in the device efficiency is demonstrated. Our approach may have implications in other semiconductor thin-film technologies.

References

[1] V.G. Karpov, A.D. Compaan and D. Shvydka, *Appl. Phys. Lett.* **80**, 4256 (2002).

[2] D. Shvydka, V.G. Karpov, and A.D. Compaan *Appl. Phys. Lett.* **82**, 2157 (2003).

[3] O. Breitenstein, K. Iwig, K. and I. Konovalov, *Phys. Stat. Sol. (a)* **160**, 271 (1997).

[4] O. Breitenstein, M. Langenkamp, *Lock-in Thermography - Basics and Use for Functional Diagnostics of Electronic Components* (Springer, Heidelberg 2003).

[5] www.thermosensorik.de.

[6] A. O. Pudov, M. Gloeckler, S. H. Demtsu, and J. R. Sites, K.L. Barth, R.A. Enzenroth, and W.S. Sampath, *Proc. 29th IEEE Photovoltaic Specialists Conference*, New Orlean 760 (2002).

[7] B.L. Sopori and R. Murphy, 12th *Eur. Photovoltaic Solar Energy Conference*, Amsterdam, The Netherlands, 1797 (1994).

[8] K. Drope and H.H. Moller, 12th *Eur. Photovoltaic Solar Energy Conference*, Amsterdam, The Netherlands, 1359 (1994).

[9] C. Christopolous, *The transmission line modeling methods*, (IEEE, New York 1995).

[10] D.W. Nileqa, X. Li, P. Sheldon, and H. Hijchst, *J. Appl. Phys.* **77**, 4489 (1995).

[11] D.J. Friedman,I. Lindau, W.E. Spicer, Phys. Rev. B **37**, 731 (1998).

[12] S. M. Sze, *Physics of Semiconductor Devices* (Willey & Sons, New York, 1981).

[13] J. G. Kushmerick, D. B. Holt, J. C. Yang, J. Naciri, M. H. Moore, and R. Shashidhar, *Phys. Rev. Lett.* **88**, 086802 (2002).

[14] P. J. Edwards and G. H. Pollard, *Phys. Rev. Lett.* **69**, 1757 (1992).

[15] P. E. Lammert, V. H. Grespi, and A. Rubio, *Phys. Rev. Lett.* **87**, 136402 (2001).

[16] G. Vignale and M. E. Flatte, *Phys. Rev. Lett.* **89**, 098302 (2002).

[17] *Handbook of Photovoltaic Science and Engineering*, eds. A. Luque and S. Hegedus (John Wiley, 2003).

[18] M. Gloeckler, A. L. Fahrenbruch, and J. R. Sites, "Numerical modeling of CIGS and CdTe solar cells: setting the baseline", *Proc. of 3rd World Conference on Photovoltaic Energy Conversion*, Osaka, Japan, May 2003, to be published.

[19] B. L. Sopori and R. Murphy, *Proc. 12th European Photovoltaic Solar Energy Conf.*, p. 1797, Amsterdam (1994); K. Drope and H. J. Moller, *ibid.*, p. 1359.

[20] D. Rose, R. Powell, U. Jayamaha, M. Maltby, *Proc. 29* [th] *IEEE Photovoltaic Specialists Conference*, New Orlean, 555 (2002).

[21] Curiously a red wine can be one of such treatments as is described in: V. G. Karpov, D. Shvydka, Y. Roussillon and A. D. Compaan, in *Proc. of 3rd World Conference on Photovoltaic Energy Conversion*, Osaka, Japan, May 2003, in press.

[22] P. V. Meyers, C. H. Liu, and T. J. Frey, U. S. Patent #4,710,589 (1987)

[23] R. H. Bube, *Photovoltaic Materials*, Imperial College Press 1998.

[24] R. Birkmire, 26th IEEE Photovoltaics Conference Proceedings 1997, p. 295

[25] S. Pruneanu, E. Veress, I. Marian, L. Oniciu, *J. of Materials Sci.*, **34**, 2733 (1999).

4. CHARACTERIZATION OF MATERIALS AND DEVICES

4.1. Photoluminescence studies

During the past year we have continued a variety of photoluminescence (PL) studies. We discuss separately 1) PL mapping under applied bias carried out as part of the "Nonuniformity" subteam of the National CdTe Team, 2)PL measurements on crystalline CdTe subjected to ion implantation of Cl, and 3) PL decay (fatigue) study. Finally, we briefly discuss 4) PL studies as part of the "Defect Chemistry/Materials Chemistry" subteam.

4.1.1. Photoluminescence (PL) mapping under applied bias

Our effort in studying the effects of nonuniformities included the National CdTe Team Meetings in Golden (November 2002) and in Golden (July 2003), where we continued to coordinate projects in the "Micrononuniformity" topical sub-team. The sub-team presented results on PL-mapping, m-EL, m-PL, m-LBIC and IR lock-in thermography.

PL mapping was aimed at characterizing changes in the degree of device lateral uniformity in fresh vs. degraded samples in both metallized and contact-free areas. Room temperature PL was excited by a 752 nm laser with the beam spot size of $\sim 80~\mu$m and step size 250 μm. We used laser intensity of ~ 1000 sun. The changes in the total PL intensity integrated from 1.38 to 1.62 eV were recorded. We studied cell prepared by three different deposition methods provided by different manufacturers: rf-sputtering (UT), VTD (First Solar, LCC.) and CSS (USF).

We observed that in general PL from under the contact area becomes dimmer and less uniform after light soak stress. Typical histograms plotted based on obtained PL maps are shown in Fig. 4.21, where bimodal distribution reflects the difference in PL intensity between contact and contact-free areas. We measured several cells of each kind and observed considerable variations even between cells prepared by the same deposition method.

It was shown[1] that a) PL is suppressed by reverse bias: electric field dominates charge carrier kinetics, b) PL saturates under strong forward bias: charge carrier kinetic is recombination-dominated, and c) PL intensity in the saturation region is extremely sensitive to device degradation. In attempt to better understand the information provided by PL mapping we extended it to mapping of cells under different applied bias (see Fig.
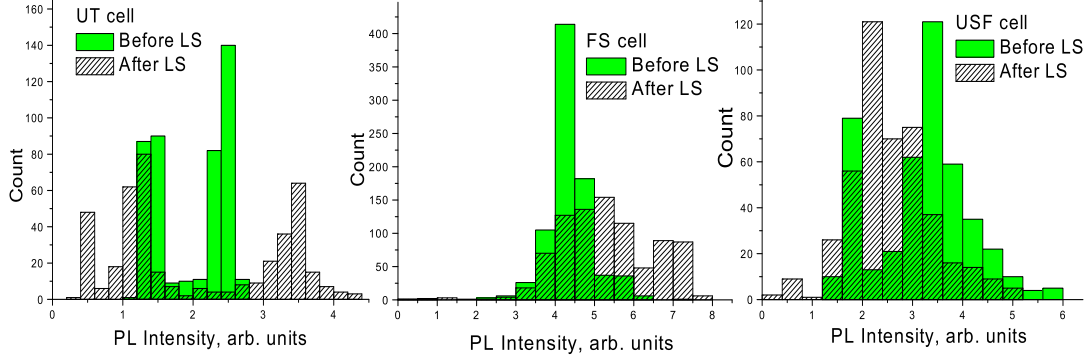
Figure 4.21: Histograms comparing PL intensity signal before and after light soak stress for 3 kind of cells prepared by rf-sputtering (UT cell), VTD (FS cell) and CSS (USF cell).
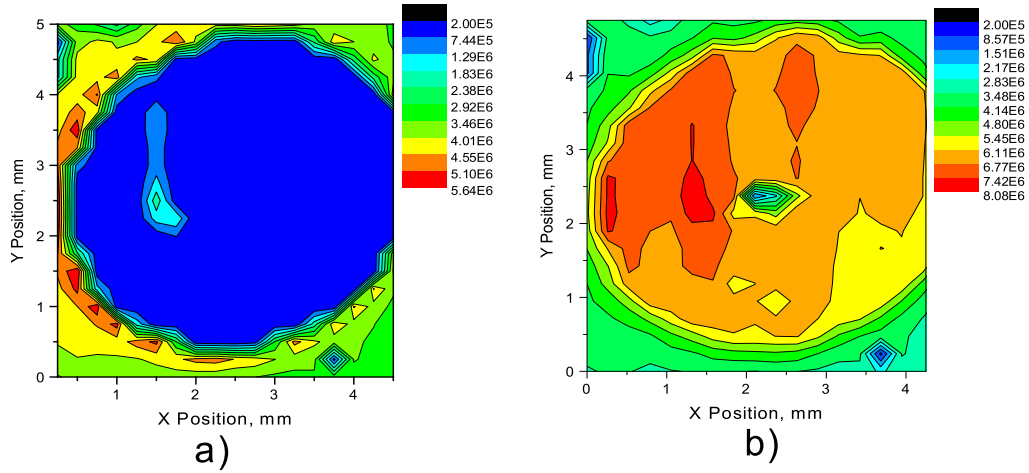
Figure 4.22: PL maps of the same rf-sputtered cell under different applied bias a) short circuit, b) forward bias of 1V.

4.22). Comparing maps measured for the same contact under different biases we were able to distinguish between typical (Fig. 4.23) and abnormal PL features.

Typical spatial PL features (Fig. 4.23) are similar at different biases implying that charge carrier kinetics is irrelevant. Most probably, PL intensity maps the absorption variations in the CdTeS alloy region, which are most likely related to variations in the alloy region thickness.

Fig. 4.24 shows some abnormal features - spots of very high or very low PL intensity. In order to understand the origin of these features it is useful to look at them at different
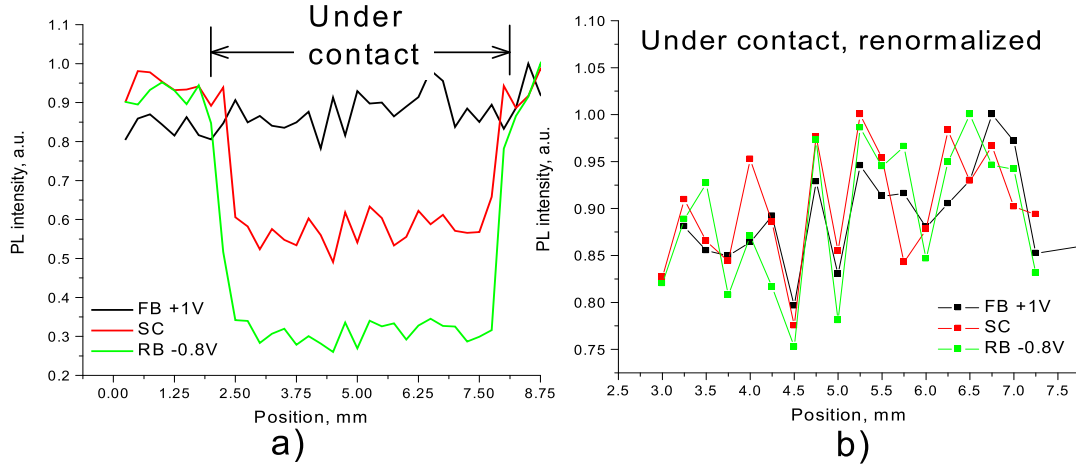
Figure 4.23: Typical features in PL map: line scans under different biases a) under contact and contact-free areas, b) part of the same line under contact, re-normalized to the same average. Line scans were obtained on the rf-sputtered cell.
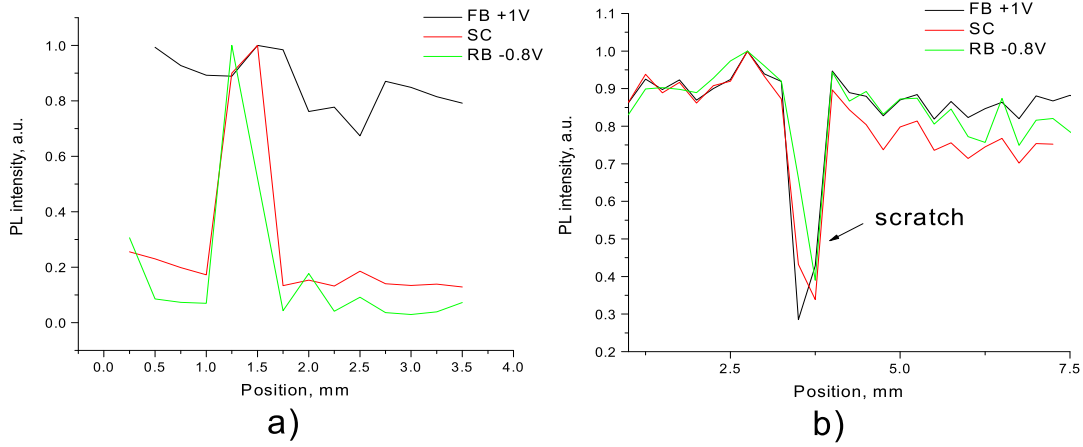
Figure 4.24: Abnormal features in PL map: line scans under different biases show features related to a) back-contact problem, b) absorber problem.

biases. For example, Fig. 4.24 a) shows high-intensity spot at RB and SC only. This kind of behavior can be related to back-contact problem: the spot does not feel applied bias. Fig. 4.24 b) shows another example of abnormally low PL intensity. Since the feature is bias-independent, it is related to damaged absorber layer (scratch).

Since photoluminescence maps the local response as opposed to, for example, electroluminescence or IR thermography, the main topography feature is related to absorption

fluctuations in the alloy region. Abnormal features are best seen under reverse bias indicative of back contact problems or damage to the absorber layer. Our conclusion is that PL mapping is very useful technique for detection of markedly problematic spots (similar to crystal wafer technology).

4.1.2. Ion implantation and PL studies of crystalline CdTe

Photoluminescence is a convenient and powerful method to probe the material properties of an operating solar cell and to investigate the defect states in the active semiconductor material, and particularly convenient for studies of the junction region. However, the unambiguous identification of the transitions responsible for the light emission, particularly in polycrystalline thin films has been elusive. Partly to address this difficulty of identification, we have performed a series of measurements on single crystals and thin films, which have received calibrated doses of known atoms from ion implantation. The disadvantage of ion implantation is that large numbers of defects are created for each atom implanted, typically 1000 displacements for each implant.

Here we report on the study of Cl implants. The ion implantation is done through collaboration with the atomic physics group at the University of Toledo on the accelerator in the Physics and Astronomy Department. Cl^{++} and Cl^{+} ions were implanted into crystalline CdTe, supplied by Keystone Crystal Co., at 3 different energies: 400, 200 and 100 keV to obtain total doses of 1.17×10^{10}, 3.9×10^{10} and 3.9×10^{11} /cm^2 (respectively 3×10^{16}, 1×10^{17}, 1×10^{18} /cm^3). The project range and range straggling are, respectively, 0.2642 and 0.1429 μm from Monte Carlo calculations using "SRIM" - The Stopping and Range of Ions in Matter).[2] These energies were chosen to match the absorption length of the 752 nm PL excitation laser. 30-minute annealing at 400 ^{o}C in N$_2$ atmosphere, using a CdTe film as a proximity cap, was done to remove most of the vacancies and interstitials produced by the implanted ions.

PL comparison at different dose on the implanted and non-implanted regions of the CdTe crystals after annealing is shown in Figure 4.25. The intensities in the whole spectrum range are enhanced by Cl doping.

Doping of CdTe with chlorine is widely used as semi-insulator for producing γ- and X-ray uncooled detectors.[3] Chlorine is known to act in CdTe in two forms: creating shallow donor

44
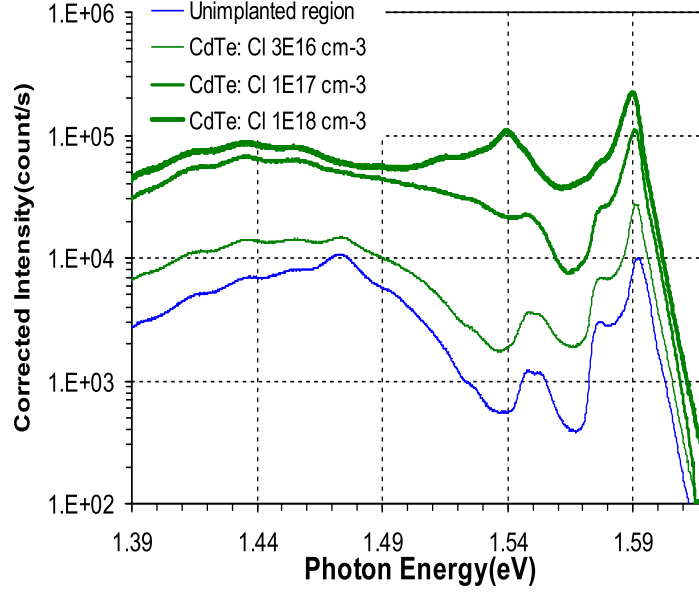
Figure 4.25: Photoluminescence on Cl implanted CdTe crystal wafer, excited by 4mW (500 sun) 752nm, for different implant doses, after annealing of damage. Free-to-band (FB) emission due to V_{Cd} at 1.475 eV disappears with increasing Cl doses (left); red shift of strongest exciton emission with increasing Cl doses (right).

levels[4–6] and acting as acceptor by creating A center, cadmium vacancy-chlorine (V_{Cd}-Cl) complexs.[7] We suggest the PL enhancement by Cl in the "defect band" of the series of peaks around 1.44 eV is due to Cl shallow donor levels. With increasing Cl doses, the strongest exciton emission shift from D^oX line at 1.592 eV to A^oX emission at 1.590eV (Fig. 4.25, right).[8] Noticing Cl should always acting as donor in CdTe, the overwhelming acceptor concentration can only be explained by formation of A centers complex. Compensation is also observed through the disappearance of 1.475 eV with increasing Cl doping (Fig. 4.25, left). This peak has not been identified before.[7] We suggest this peak is arising from V_{Cd} and disappears due to the introduction of Cl and A centers formation. Several studies[9] have identified acceptor-related exciton A^oX line connecting to chlorine A center in Cl doped CdTe single crystal. Dramatic PL intensity enhancement due to Cl impurity is not seen in other studies and could be used as a convenient method for tracing Cl in CdTe.

This effort on ion-implanted CdTe crystals and films is continuing with the implantation of other atomic species, particularly those anticipated being important as acceptors and

donors in CdTe cells.[10]

4.1.3. PL fatigue and related degradation

Photoluminescence (PL) technique, often used to judge the material quality, is typically assumed to be a non-destructive method. This assumption does not always hold. In this work we find that in a polycrystalline CdTe/CdS solar cell, illuminated with a laser beam of constant power, junction photoluminescence intensity gradually decreases over time. This phenomenon is similar to the PL fatigue observed in chalcogenide glasses[11,12] and a number of other systems, such as GaAs[13–16], GaN[17], amorphous and porous Si[11,18,19], and quantum wells[20].

In the latter work, the observed fatigue amplitude was in some cases rather significant, up to 90% of the initial PL intensity during $\sim 100 \div 1000$ seconds, depending on the material, laser beam intensity, and temperature. No comparison between materials has been attempted and in each publication the PL fatigue was interpreted as though it was unique to a given system. Exponentials[12,16], stretched exponentials[18,19], and powers[14] were used to fit the fatigue temporal dependencies. One general believe in the above-cited work is that PL fatigue is due to defect accumulation. More specific hypotheses vary between different authors.

However, we note that overall, the fatigue kinetics data for different materials look similar. Hence, the same physical mechanism can be suspected behind the phenomenon in a variety of materials. Proposing such a mechanism is one of the goals here.

Experimental   We conducted our experiment on CdTe/CdS solar cell made by vapor transport deposition as described in Refs. 21,26. These cells are thin-film junctions sandwiched between two electrodes, of which one is the transparent conductive oxide (TCO, ρ=15 $\Omega/\square$) and the other is a metal of negligibly small resistance. Some of this structures remained unfinished, without a metal contact on top of CdTe layer. This provision made it possible to study the back contact effect on PL decay (it was shown indeed[22] that the presence of surface metal can effect the PL signal).

PL was excited from the glass side with 752 nm line of Kr laser. In this case, CdS is transparent to the laser light, which is absorbed in CdTe with an absorption length of ~ 0.3

μm. This is much narrower than the depletion layer width $\sim 1 \div 3$ μm in the lightly p-doped CdTe. Hence, both the absorption and emission are restricted to a narrow junction region. The laser beam diameter was less than 0.1 mm. PL intensity change with time was recorded with CCD camera for several different temperatures and laser intensities.
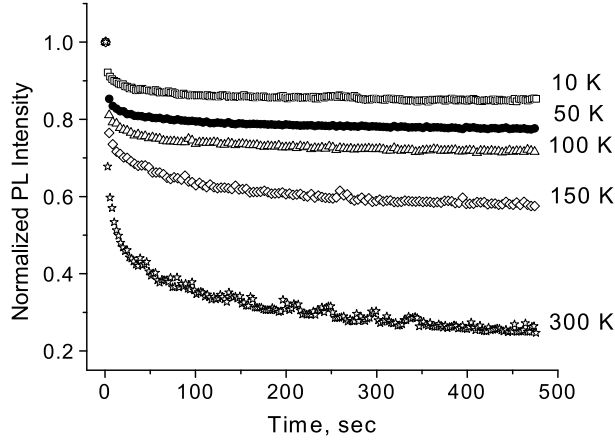
Figure 4.26: Raw data on PL fatigue including laser heat contribution. Measured under the contact, laser power 25 mW ($\sim$ 1000 sun).

We start with separating out the PL fatigue from the concomitant heat induced PL decrease. Shown in Fig 4.26 is an example of 'raw' data corresponding to different temperatures. Each of the curves shows relatively fast initial drop followed by more gradual decay. The initial drop rather independent on the sample temperature was attributed to the laser heating effect on the temperature dependent PL intensity in CdTe film as explained below. We find it important to subtract the laser heating effect, which otherwise masks the PL fatigue trends and makes it hard to interpret.

The reasoning behind the laser heat subtraction is that (i) the PL intensity in CdTe has a considerable temperature dependence (as verified in Fig. 4.27) and (ii) the characteristic time of establishing the stationary temperature distribution ($\sim$ 1 s, see the Appendix) is comparable to that of the observed initial PL intensity drop in Fig 4.26.

To additionally verify the laser heat effect on PL intensity we implemented a setup where the sample was placed on a moving stage. In this setup the laser beam spot moved relative to the stage by a distance of its diameter in a time of the order of 0.5 s, shorter than the characteristic temperature equilibration time. At room temperature we observed the PL intensity drop by the factor of 1.5 in a matter of seconds after the stage seized to move.

47
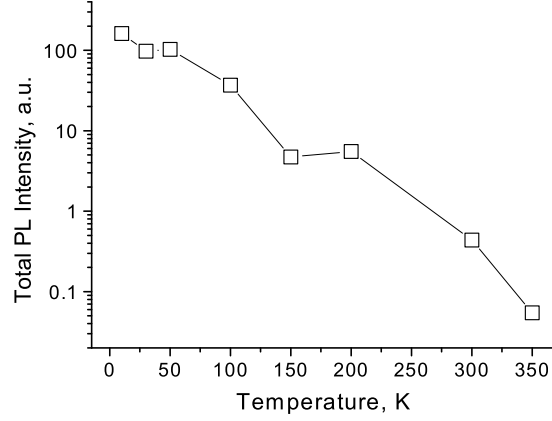
Figure 4.27: Temperature dependence of total PL intensity in CdS/CdTe device.

This is consistent with the laser heating effect: the beam fixed on a particular spot increases the spot temperature, thus decreasing PL, in accordance with the data in Fig. 4.27.
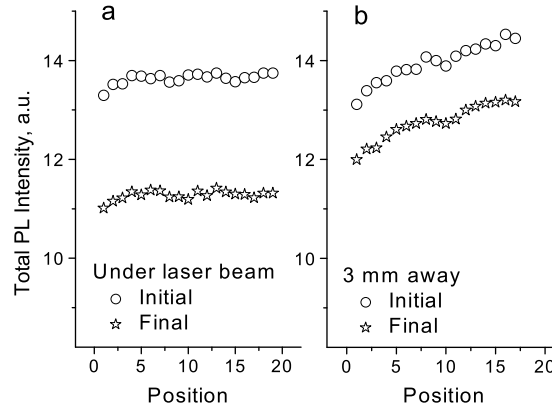
Figure 4.28: Degradation of PL signal in laser cycling experiment a) directly under laser beam vs b) 3 mm away from the laser beam. Horizontal axes show the laser beam position along the scan line.

Using the same setup we were able to verify the nonlocal character of PL fatigue in the course of cyclical laser beam scanning as follows. First, we measured PL intensity along two parallel lines 3 mm apart on the sample. Then we performed periodical laser scanning along one of these lines. After 12 cycles we detected PL fatigue not only along the scanned line, but also along the unstressed second line (Fig. 4.28). The latter nonlocal PL fatigue effect can be understood assuming that the decrease is due to material degradation caused by the laser-generated nonequilibrium charge carriers, which as shown in Ref. 23 propagate

48

far from the laser beam in the lateral direction. The fact that the nonlocal effect was weaker we attribute to the laser-induced heating with relatively short localization radius (see the Appendix): higher temperature directly under the beam lead to the fatigue acceleration along the laser trajectory line.
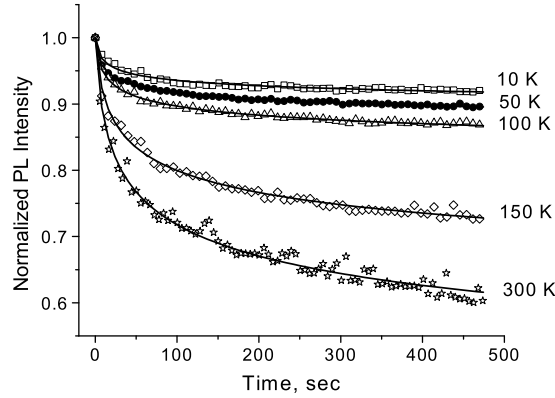
Figure 4.29: Data on PL fatigue without the laser heating effect. Contact area, laser power 25 mW. Solid lines represent fits by Eq. (4.38) and Eq. (4.39).

Shown in Fig. 4.29 is a set of typical PL fatigue data corrected to the laser heating effect and normalized to the initial PL intensity. Our heating subtraction procedure was based on the observed drastic change in logarithmic derivatives of the PL decay temporal dependencies. We identified that change with the characteristic temperature equilibration time and eliminated the data corresponding to shorter times.

We observed the following trends: (1) the fatigue accelerates and its amplitude increases with temperature and laser beam power; (2) there are considerable variations in the PL fatigue amplitude (up to 100%) between different spots on the sample, especially for metal-free area (consistent with the observed fluctuations in solar cell efficiency degradation[24]); (3) there is no significant difference in the fatigue kinetics between metal-free and metallized regions; (4) the fatigue spreads beyond the laser spot region affecting areas up to several mm away from the spot; (5) PL fatigue kinetics are not very different in the open circuit and shorted samples, in spite of the fact that the former shows considerably higher PL intensity.[1]

Some of the above items, such as beam power dependence and nonlocal degradation, are similar to the observations for other materials. Other facts, such as variations between different spots and independence of back contact are observed here for the first time.

49

Model We attribute the observed PL fatigue to defects generated under illumination. While photons do not have enough energy to create the defects, the light-generated electrons and holes are capable of defect generation, which is considered a mechanism underlying photo-induced degradation in many cases[23]. In particular, it was experimentally verified for the case of CdTe photovoltaics that light-generated electrons and holes, rather than the light per se, are responsible for degradation.[26]

In the simplest approximation the defect generation rate is linear in the charge carrier concentration n (a defect is generated by capturing single electron or hole on some cite) that is

$$\frac{dN}{dt} = \alpha n - \beta N. \tag{4.28}$$

Here α and β are material parameters, the two terms in the right-hand side describe defect creation and annihilation. In turns, the electron kinetics depends on defect concentration (N) and built-in junction electric field $\mathcal{E}$,[1]

$$G(x) = \gamma n N + \mu \mathcal{E} \frac{\partial n}{\partial x}. \tag{4.29}$$

Here

$$G(x) = G_0 \Theta(x) \exp(-x/l)$$

is the electron-hole generation rate ($\text{cm}^{-3}\text{s}^{-1}$), l is the absorption length, μ is the mobility, $\Theta(x)$ is the step function ($x > 0$ corresponds to CdTe), γ is a constant. In the right-hand side of Eq. (4.29) the first term accounts for the electron recombination via defects, while the second one describes the charge carrier drift caused by the junction electric field. In Eq. (4.29) we have taken into account that the electron kinetics is fast (as compared to that of the defects) and thus can be described in the quasistationary approximation.

Eqs. (4.28) and (4.29) reduce to a complex mathematical problem that in the generation region $x \leq l$ can be simplified by employing the approximations[27]

$$G(x) = const \equiv G, \quad \frac{1}{n}\frac{\partial n}{\partial x} = l^{-1}. \tag{4.30}$$

As a result Eq. (4.29) takes an intuitively clear form

$$n = G\tau, \quad \frac{1}{\tau} = \frac{1}{\tau_N} + l^{-1}\mu\mathcal{E}, \tag{4.31}$$

where the two last terms describe the probabilities per unit time for the carrier to recombine non-radiatively ($1/\tau_N \equiv \gamma N$) or to be swept out by the field from the generation region.

Eqs. (4.28) and (4.31) have a closed solution which is still arithmetically cumbersome. To make it more intuitive we start with considering the fatigue early stage. Neglecting the annihilation term in Eq. (4.28) gives

$$n(t) = n_0 \left(1 + \frac{t}{\theta} \right)^{-1/2} \tag{4.32}$$

where

$$n_0 = \frac{G\tau_0}{1 + l^{-1}\mu\tau_0\mathcal{E}}, \quad \theta = \frac{G}{2\alpha\gamma n_0^2}. \tag{4.33}$$

Here $\tau_0 \equiv 1/\gamma N_0$ and N_0 is the initial defect concentration.

Furthermore, the initial stage of fatigue can be similarly described for a higher order kinetics, $dN/dt = \alpha n^\eta$ to give

$$n(t) = n_0 \left(1 + \frac{t}{\theta} \right)^{-1/(\eta+1)}, \quad \theta = \frac{G}{\alpha\gamma(\eta+1)n_0^{\eta+1}}. \tag{4.34}$$

We observe that functionally the temporal kinetics is field-independent. However, its characteristic time, θ depends on the field via the initial carrier concentration, in accordance with Eq. (4.33).

Note that the temporal dependence in Eq. (4.34) was successfully used to fit the PL fatigue in GaAs.[14] From more general prospective, it is important that the built-in electric field does not affect the shape of the initial PL fatigue temporal kinetics. In particular, this makes our consideration applicable to some crystals where short absorbtion length restricts PL to a near surface region of significant electric field.[13,16] As long as the electric field does not affect the kinetics, the data corresponding to different systems (bulk PL, near-surface PL, junction PL) can be all analyzed within the same framework.

The fatigue late stage can be described by setting the time derivative zero in Eq. (4.28), which gives the saturated charge carrier concentration n_s,

$$n_s = \frac{G}{\gamma N_\infty} \left\{ \left[\left(\frac{\mu\mathcal{E}}{2\gamma l N_\infty} \right)^2 + 1 \right]^{1/2} - \frac{\mu\mathcal{E}}{2\gamma l N_\infty} \right\} \tag{4.35}$$

Here

$$N_\infty = \left(\frac{\alpha G}{\gamma\beta} \right)^{1/2}. \tag{4.36}$$

is the ultimate defect concentration accumulated after infinitely long time in the absence of field. Note that in a strong field, $\mathcal{E} \gg \gamma l N_\infty/\mu$ the carrier concentration does not degrade,

$n_s = n_0 = Gl/\mu\mathcal{E}$. In a rough approximation, the charge carrier evolution can be described by combining Eqs. (4.32) and (4.36),

$$n(t) = (n_0 - n_s)\left(1 + \frac{t}{\theta}\right)^{-1/2} + n_s. \tag{4.37}$$

We attribute the observed PL fatigue to the time decay in the charge carrier concentration and assume the radiative recombination kinetics bilinear in the electron and hole concentrations, $I \propto n_e n_h$. In particular, using Eq. (4.33) to describe n_e and n_h gives an accurate result for the bias-dependent PL intensity[1].

While I is bilinear in $n_e n_h$, the two type carrier kinetics can be significantly different owing to the difference in their parameters. For example, the hole drift mobility in CdTe is by order of magnitude lower than that of electrons. In addition, holes typically stronger interact with the atomic system thus being more capable of creating the defects. Therefore, the details of the fatigue kinetics can be different in different systems depending on the charge carrier parameters.

From this point on we narrow the model to reflect the specificity of our data. The key observation is that the fatigue kinetics is almost the same under open- and short-circuit cases. Hence, the junction electric field, different for the above two cases, does not affect the defect generation and underlying charge carrier kinetics (we recall that PL is emitted from the junction region).

On the other hand, the bias dependent PL exhibits a seemingly conflicting observation of the charge carrier kinetics sensitive to the junction electric field.[1] To reconcile the two facts we attribute them to two different types of carriers, electrons and holes, which reaction to the field and defect generation abilities can be significantly different. It is likely that mobile electrons are effectively swept away by the field, while the holes spend more time in the junction region and generate defects causing the PL fatigue.

Consider the extreme case where the carriers of one type (n_h) are immobile and fully responsible for defect generation, while the alternative mobile carriers (n_e) are swept away from the junction region. In this case the PL intensity can be represented as

$$I(t) \propto n_h(t)n_e(0) \propto \frac{n_h(t)}{1 + l^{-1}\mu_e\tau_{0e}\mathcal{E}}, \tag{4.38}$$

where $n_h(t)$ is given by Eq. (4.32) or Eq. (4.39) below. This form enables one to simultaneously describe the bias-dependent PL intensity and PL fatigue.

Assuming the fatigue kinetic field independent, Eqs. (4.28) and (4.31) can be solved for n to give[21]

$$n = \frac{G}{\gamma N_\infty} \left\{ 1 - \left[1 - \left(\frac{N_0}{N_\infty} \right)^2 \right] \exp\left(-2\beta t\right) \right\}^{-1/2}.$$

(4.39)

When the time is relatively short, $\beta t \ll 1$ the latter result takes the form of Eq. (4.32) with

$$\theta \equiv \frac{1}{2\beta} \frac{N_0^2}{N_\infty^2 - N_0^2}.$$

(4.40)

Note that θ is generally temperature dependent as it includes the coefficients α (through N_∞), and β which describe the probability of electron-triggered atomic rearrangements. The typical dependence of that kind is thermally activated above the Debye temperature and is weaker at lower temperatures.[28]

Fitting the data   Assuming, on empirical grounds, a significant asymmetry between the electrons and holes we used Eq. (4.38) with Eq. (4.39) for $n_h(t)$ to fit the data. As shown in Fig. 4.29, good agreement is achieved.
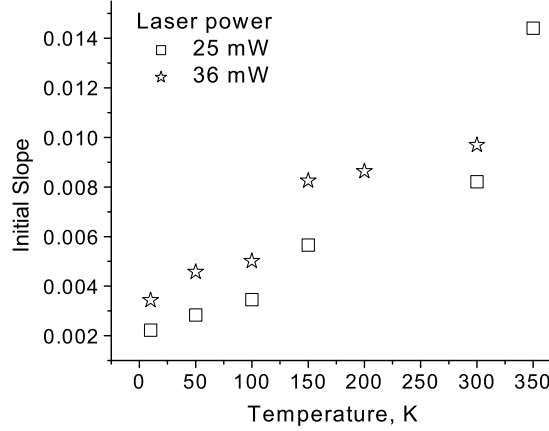
Figure 4.30: Dependence of the initial PL fatigue slope on temperature for different laser beam powers.

We have verified several predictions of the above model addressing the main curve parameters, the fatigue initial slope $(d \ln I / dt = 1/2\theta)$ and relative saturated value $(I(\infty)/I(0))$ versus temperature and generation rate G proportional to the laser power in our experiment. The predictions are:

$$\frac{1}{2\theta} = \beta \left[\left(\frac{N(\infty)}{N(0)} \right)^2 - 1 \right] = \beta \left(\frac{\alpha G}{\gamma \beta N_0^2} - 1 \right),$$

(4.41)

53
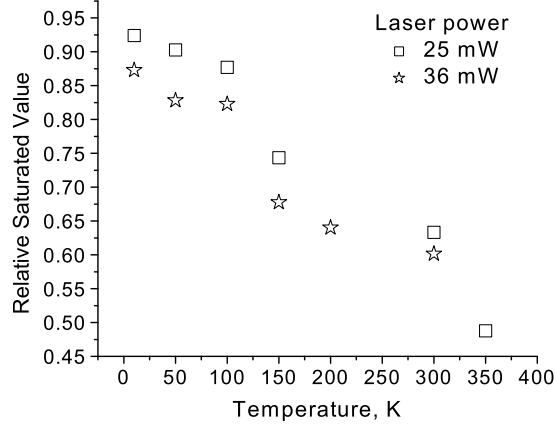
Figure 4.31: Temperature dependence of the relative saturated value for different laser beam powers.
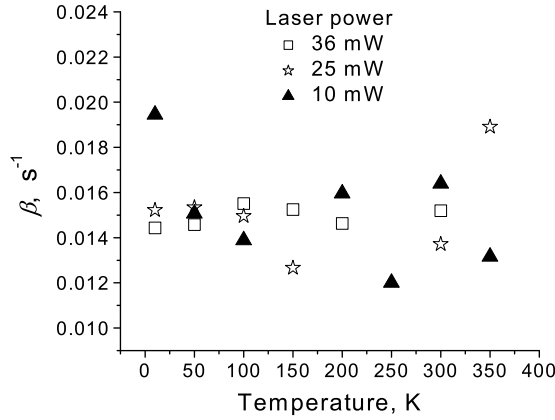
Figure 4.32: Probability of defect annihilation β vs. temperature: independent of laser power.

$$\frac{I(\infty)}{I(0)} = \frac{N(0)}{N(\infty)} = \left(\frac{\gamma \beta N_0^2}{\alpha G} \right)^{1/2}. \tag{4.42}$$

The data in Figs. 4.30, 4.31 are qualitatively consistent with Eqs. (4.41), (4.42), which predict increase in the initial slope and decrease in the relative saturated value with T and G. We note that the above relations combine into

$$\frac{1}{2\theta} \left[1 - \left(\frac{I(\infty)}{I(0)} \right)^2 \right]^{-1} = \beta \tag{4.43}$$

where the right-hand-side can depend on T, but not on G. The latter prediction is verified in Fig. 4.32, where temperature dependence is obscured by spot-to-spot PL fatigue variations (note, that each point in Fig. 4.32 is taken at a different spot on the sample).

54

Related degradation phenomena Closely related to the PL fatigue is the phenomenon of light-induced degradation known to be a significant problem for thin-film photovoltaics. A minor difference is that sun light has a broad spectrum and thus generates the nonequilibrium charge carriers more uniformly in space. In the uniform generation approximation, l in the above equations represents the junction thickness rather than the absorption length. Also, for the case of practically important relatively small degradation, the photovoltaic characteristics change approximately linear with the charge carrier concentration. With these modifications, and generalizing Eq. (4.34) the relative degradation of the major photovoltaic parameters X, such as short circuit current ($X = J_{sc}$), open circuit voltage ($X = V_{oc}$), and efficiency ($X = E$) will all have the same temporal dependence

$$\frac{\Delta X}{X} \propto \left(1 + \frac{t}{\theta}\right)^{-\eta/(\eta+1)}, \quad \theta \propto \frac{(1 + \mathcal{E}/\mathcal{E}_c)^{\eta+1}}{\alpha \gamma G^\eta}. \tag{4.44}$$

Here the characteristic field $\mathcal{E}_c \equiv l/\mu\tau_0$ is related to the recombination time, which is known to depend on the carrier generation rate[29]. In particular, $\mathcal{E}_c$ can be much lower (and τ_0 much longer) far from metallurgical junction. Correspondingly, the sun light induced degradation can be more sensitive to the electric field than PL fatigue.

Eq. (4.44) contains a number of verifiable predictions. (i) Specific temporal dependence with a tendency to saturation. (ii) Temperature dependence of the time scale θ related to the product $(\alpha\gamma)^{-1}$ exponential in T at temperatures higher or of the order of the Debye temperature (Note that the latter dependence is not predicted for the absolute value of degradation, whose temperature dependence is often addressed.[30]) (iii) Field dependence, which predicts the short circuit device (maximum $\mathcal{E}$) to degrade less than the open circuit one ($\mathcal{E}$ is suppressed), consistent with observations.[31,32]

From the practical standpoint, it is important that a variety of charge carrier driven degradation phenomena possess the same temporal, field, and temperature dependencies. This opens a venue for predictive modelling and accelerated life testing where one source of degradation is replaced by another, for example, relatively fast laser or electron beam induced degradation instead of long term one-sun-light degradation. As an illustration, in Fig. 4.33 we compare properly rescaled degradation kinetics caused by all three of the latter sources: good qualitative agreement is observed.[33]

A comment is in order regarding charge carrier triggered degradation in laterally nonuniform systems.[26] The nonuniformity screening by charge carriers depends on their
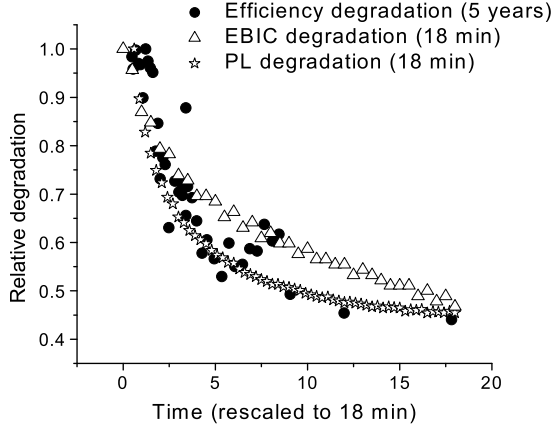
Figure 4.33: Comparison of the light-induced (1 sun) efficiency degradation, e-beam-induced (15 keV) EBIC degradation and laser-beam-induced (1000 sun) PL degradation. Data re-scaled to 18 min.[33]

concentration,[23] which is different for different sources. This will eventually result in the correspondingly different degradations. Indeed, the nonuniformity showed up in our experiments as considerable fluctuations in the fatigue effect between different spots. The above idea of accelerated life testing cannot be deterministically predictive for nonuniform systems, such as amorphous, porous, and polycrystalline materials. However, for such systems the accelerated testing results interpreted statistically may characterize the trends in degradation phenomena.

Conclusions   In conclusion, the decay in the PL excited by a stationary laser beam in CdTe photovoltaics is for the first time observed. Two decay sources are identified: short-term laser induced heating decreasing PL intensity, and long-term material degradation (fatigue) due to photoinduced defect accumulation. The fatigue exhibits such trends as acceleration with the temperature and light intensity, considerable variations between different spots on the sample, and nonlocal nature of the effect. Similarities with the PL fatigue in a number of other systems are found. Our theoretical model gives correct predictions about the fatigue temperature, light intensity, and field dependencies.

Our understanding predicts the same physics underlying nominally different degradation phenomena, such as caused by the laser beam, electron beam, and sun light. This opens a venue for accelerated life testing where long term sun-light induced degradation is simulated

by short term degradations caused by laser or electron beams, or electric bias. The similarity can be obscured by material nonuniformity effects. More study is called upon to clarify this practically important issue.

Appendix In this appendix we consider the temperature distribution caused by the laser beam, which we model as a cylindrical heat source across the film of small thickness h attached to a relatively thick metal slab ('cold finger') of thickness H. The thermal conductivities of the two materials are κ and K respectively (Fig. 4.34). The temperature T_0 is maintained at the opposite side of the system. We assume the heat source of small radius as compared to the below derived thermal nonuniformity decay length λ. The heat transfer is then described by the equation

$$h\kappa\frac{1}{r}\frac{\partial}{\partial r}r\frac{\partial T}{\partial r} = -K\frac{T - T_0}{H}, \tag{4.45}$$

where r is the distance from the cylinder axis. This gives the temperature decay length

$$\lambda = \sqrt{\frac{\kappa}{K}Hh} \tag{4.46}$$

For numerical estimates at room temperature we take $k \approx 0.1$ W/cm-^{o}C, $h \sim 3$ μm and consider copper slab of $H = 1$ cm and $K \approx 4$ W/cm-^{o}C. This gives $\lambda \sim 0.03$ mm, larger than our laser beam radius.
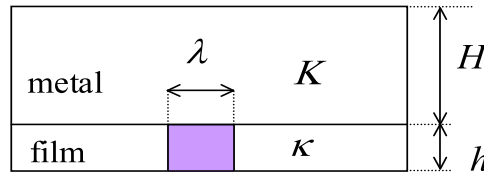
Figure 4.34: Parameters describing heat transfer from a cylindrical source in thin film in contact with a metal slab.

To estimate the temperature nonuniformity amplitude δT caused by a source of power P consider the heat transfer equation

$$P = 2\pi\lambda h\kappa\frac{\partial T}{\partial r} \approx 2\pi h\kappa\delta T. \tag{4.47}$$

For typical $P \sim 10$ mW this gives $\delta T \sim 50$ K.

Finally, to estimate the thermal conduction equilibration time

$$\tau \sim \frac{H^2 C \rho}{K} \qquad (4.48)$$

we use the copper specific heat $C \approx 400$ J/kg-K and the density $\rho \approx 10$ g/cm^3, which give $\tau \sim 1$ s.

4.1.4. Defect chemistry studies

As a part of the National CdTe team we participated in the Defect/Materials Chemistry sub-team activity. Our task was to perform low-temperature PL measurements on VTD cells which had been light soaked for 45 days under different bias conditions and to try to identify defects formed during the stress. The sub-team leader - First Solar, provided these samples. We presented the results of our study during the CdTe teaming meeting in Golden (July, 2003).

4.2. Admittance spectroscopy: single defect admittance and displacement current

Admittance spectroscopy is one of the major semiconductor diagnostic techniques. It has several modifications[34–36], of which the capacitance - voltage $(C - V)$ and admittance - frequency $(Y - \omega)$ are most known. The $C - V$ profiling tests the spatial charge distribution. Frequency dependent admittance $Y(\omega)$ is generally attributed to defects. Indeed, because in response to the testing ac electric potential, defects change their occupation numbers depending on their relaxation times, they have frequency dependent charge storing ability. In spite of numerous applications, the $Y(\omega)$ data are not fully understood. The interpretation lacks basic concepts that would apply to an arbitrary system/model and discriminate between major features and minor details. For example, the displacement current component is commonly missed in the calculated admittance; the existing models do not contain the geometrical capacitance limit; there is no direct way to estimate the number of contributing defects from the data. In this work we try to put the admittance spectroscopy interpretation on more solid basis. We introduce a single defect impedance concept, which facilitates the data interpretation, and pay special attention to taking the displacement current into consideration. We derive the formula for admittance that applies to any system, contains the

geometrical capacitance limit, and establishes the domains of applicability of the existing models.
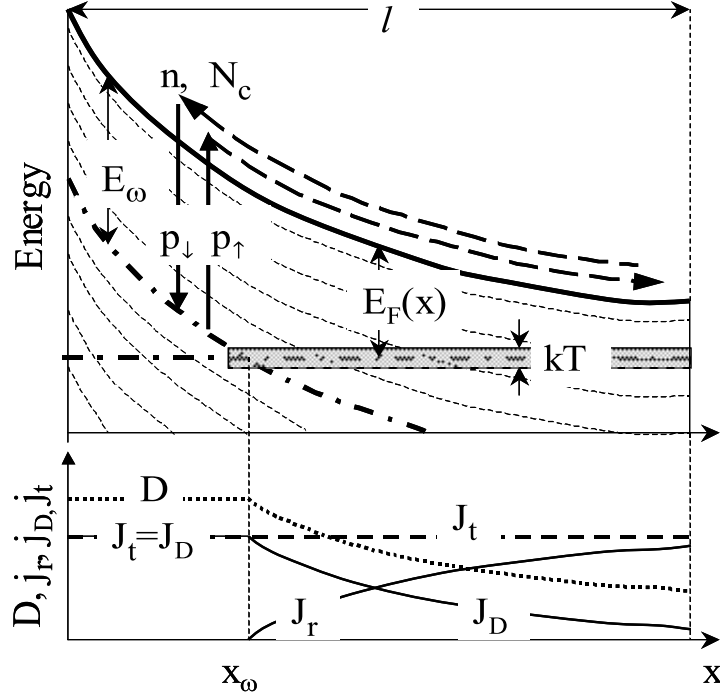
Figure 4.35: *Top*: Energy band diagram for defect states and related processes in the Schottky barrier. Thin dashed lines represent defect levels of different energies. Solid and dashed arrows show respectively trapping - detrapping processes and related electron currents. Other notations are explained in text. *Bottom*: spatial distributions of the electric induction (D), total current (J_t) and its real (J_r) and displacement (J_D) components.

Elemental defect capacitance We start with intuitive explanation of a single defect capacitance based on the band diagram (Fig. 4.35) that includes a number of defect levels and band bending caused by external bias or contact potential. In particular, it can represent a Schottky barrier[37] or a part of p-n junction. Consider a defect level with the energy E_ω below the band edge. A small testing ac voltage $U = U_0 \exp(i\omega t)$ modulates the free carrier concentration in the proximity of defect. This can be equally expressed in terms of the local quasi-Fermi level modulation, $\delta E_F = qU$ where q is the electron charge. To begin, we assume the defect relaxation time to be short, $\omega\tau \ll 1$. Then, the defect occupation will

adiabatically follow δE_F,

$$\delta f = (-\partial f/\partial E)\delta E_F = f(1-f)\delta E_F/kT,$$

where $f = \{1 + \exp[(E_F - E)/kT]\}^{-1}$ is the Fermi distribution. The change in occupation number induces the current,

$$j = q\frac{\partial \delta f}{\partial t} = i\omega C_0 U, \qquad (4.49)$$

where, in accordance with Ohm's law, we have introduced the elemental quasi-static ($\omega\tau \ll$ 1) defect capacitance

$$C_0 = f(1-f)\frac{q^2}{kT}. \qquad (4.50)$$

C_0 is independent of defect structure and equally applies to the electrons and holes being invariant with respect to the change $f \to 1 - f$, $q \to -q$.

Note that while the expression for C_0 seemingly diverges with $T \to 0$, the relaxation time τ simultaneously increases thereby violating the condition $\omega\tau \ll 1$ under which Eq. (4.50) holds; this is taken into account in what follows . Note also that the same result for C_0 follows from the differential capacitance definition $C = qd\delta f/dU$.

A comment is in order regarding the physical meaning of the above result. While it has a 90 degree phase shift from the applied field, the current j in Eq. (4.49) is related to the real charge transfer as illustrated in Fig. 4.35. This should not be mixed with the displacement current that occurs without real charge transfer [taken into account below; see Eq. (4.61)], which standard electrodynamic definition[38] is $J_D = \partial D/4\pi\partial t$ where D is the electric induction. The difference is clearly seen from an example of the standard flat plate capacitor where the above derived 'defect' current is absent, while the displacement current determines the geometrical capacitance value $C_g = J_D/i\omega U$.

C_0 is relatively small beyond a narrow band $\sim kT$ near E_F because neither strongly populated ($1 - f \ll 1$) nor empty ($f \ll 1$) defects can significantly change their occupation numbers in response to a small perturbation. It has a sharp maximum for defects with $E = E_F$ (i. e. $f = 1/2$). By way of illustration, the maximum defect capacitance $(C_0)_{max} \equiv q^2/4kT$ is $2 \cdot 10^{-18}$ F at room temperature, which coincides with the capacitance of a 140 Å radius metal sphere.

Note that the importance of the length q^2/kT has long been recognized in connection with the electron scattering and capturing by charged centers in solids. However, it is for the

first time here that this length is related to the capacitance. A simple physical explanation of the 'elemental' capacitance q^2/kT is that the defect changes its charge by $\sim q$ in response to the electric potential variation $\sim kT/q$.

Single defect admittance It is straightforward to extend the above consideration to arbitrary $\omega\tau$. This will be shown to result in the concept of defect admittance, which quantity has both real (conductance) and imaginary (capacitance) parts.

We start by clarifying the assumption of E_F modulation being the primary defect recharging source. This is justified by noting that $E_F = T\ln(N_c/n)$ where N_c is the effective concentration of states in the band and the free carrier concentration n oscillates almost independently of defect recharging. The latter independence reflects the fact that the free carrier relaxation time (of dielectric nature) in the external field is typically much shorter than τ. We therefore assume that the free electrons adiabatically follow the testing perturbation and recharge the defect states.

We shall now introduce the defect admittance $y \equiv j/U$ where, generally speaking, the defect current j contains both the imaginary and real parts. Following the above consideration, the admittance imaginary part divided by $i\omega$ is called the defect capacitance, while its real part is the defect conductance. We start with the balance equation that describes the defect recharging rate,

$$\frac{\partial f}{\partial t} = n(1-f)p_\downarrow - fp_\uparrow N_c. \tag{4.51}$$

Here $p_\downarrow$ and $p_\uparrow = p_\downarrow exp(-E/kT)$ are the electron trapping and detrapping probabilities $(\mathrm{cm^3 s^{-1}})$. To solve the latter equation we substitute there the standard presentation for the time modulated quantities

$$n = n_0 + \delta n_0 \exp(i\omega t),$$
$$f = f_0 + \delta f_0 \exp(i\omega t), \tag{4.52}$$
$$qU = \delta E_F = -kT\delta n_0 \exp(i\omega t)/n$$

where modulation amplitudes are considered small, $\delta n_0 \ll n_0$ and $\delta f_0 \ll f_0$. Linearizing Eq. (4.51) with respect to δn_0 and δf_0 and introducing the defect relaxation time

$$\frac{1}{\tau} = p_\uparrow N_c + p_\downarrow n, \tag{4.53}$$

61

yields the equation for the defect occupation number

$$\delta f_0 = \frac{1}{1+i\omega\tau}\frac{C_0 U}{q}. \tag{4.54}$$

Calculating the current $j = q\partial f/\partial t$ gives the defect admittance,

$$y \equiv \frac{j}{U} = G + i\omega C, \tag{4.55}$$

where the defect conductance (G) and capacitance (C) are introduced as

$$G = C_0\frac{\omega^2\tau}{1+(\omega\tau)^2}, \quad C = \frac{C_0}{1+(\omega\tau)^2}. \tag{4.56}$$

The latter quantities are related to the defect relaxation time and energy level position (through the definition for C_0) and are not sensitive to its microscopic structure.

Screening   The original testing field is screened due to defect recharging (we neglect the free carrier redistribution). This is described by the Poisson equation

$$\frac{d^2U}{dx^2} = -\frac{4\pi q}{\epsilon}\int \delta f_0(E)g(E)dE, \tag{4.57}$$

where $g(E)$ is the defect density of states and ϵ is the dielectric constant. Substituting here Eqs. (4.54) and (4.50) yields

$$\frac{d^2U}{dx^2} = \frac{U}{L^2}, \quad \frac{1}{L^2} = \frac{4\pi q^2 g[E_F(x)]}{\epsilon\{1+i\omega\tau[E_F(x)]\}} \tag{4.58}$$

where L is the screening length. Such screening has long been known for $g(E) = const$ in the static limit where[39] $L = L_0 = \sqrt{\epsilon/4\pi q^2 g}$. The two qualitatively different regimes of screening are that of (i) mono-energy defect level, $g(E) = N\delta(E - E_\omega)$ and (ii) continuous density of states.

For the case (i) we integrate Eq. (4.58) from $x_\omega - \delta$ to $x_\omega + \delta$, $\delta \to 0$ where the point x_ω is defined by $E_F(x) = E_\omega$ (see Fig. 4.35). We take into account that $\delta(E - E_\omega)|dE_\omega| = \delta(x - x_\omega)|dx|$ and that the static electric field $dE_\omega/qdx = 4\pi q N x_\omega/\epsilon$. This gives a stepwise change

$$\delta\mathcal{E} = \frac{\mathcal{E}}{1+i\omega\tau}. \tag{4.59}$$

in the testing field $\mathcal{E} = -dU/dx$. In the static limit $\omega\tau \ll 1$ the field is completely screened at the boundary $(x = x_\omega)$ between filled and empty states. At not very small frequencies the field penetrates infinitely deep and has the opposite-phase (capacitive) component.

For the case (ii) of continuous $g(E)$ we use the standard representation $\tau = \tau_0 \exp(E/kT)$ and introduce the demarcation energy[35]

$$E_\omega = kT \ln \left(\frac{1}{\omega \tau_0} \right), \tag{4.60}$$

separating 'fast' $(E < E_\omega)$ and 'slow' $(E > E_\omega)$ states. The corresponding spatial separation occurs at x_ω (see Fig. 4.35). The 'slow' states give almost no contribution to screening, while the 'fast' ones are described in the static limit; a narrow transitional band $E_\omega \pm kT$ is immaterial.[40] Using the static screening length we conclude that the field penetrates infinitely deep when $L_0 > x_\omega$ and is significantly screened when $L_0 < x_\omega$.

Integral admittance The integral admittance $Y = J_t/U_t$ is defined through the integral current (J_t) and total potential drop (U_t) across the system. In calculating J_t we note that the defect recharging current J_r is due to real charge transfer. Taking into account also the displacement current J_D the total current per unit area $J_t = J_r + J_D$ can be presented in the form

$$J_t = \int dx g(E_F(x)) U(x) y(E_F(x)) + \frac{\partial D(x)}{4\pi \partial t}. \tag{4.61}$$

Naturally, J_t is independent of x, which can be verified by using $D = -\epsilon \partial U / \partial x$ and Eq. (4.58). This means, in particular, that in the regions where defects are fully ionized and do not change their charge states, the system admittance is of entirely displacement current nature, similar to the well known flat plate capacitor case.

As is shown in Fig. 4.35, the defect recharging is suppressed and the current is of entirely displacement nature, $J_t = J_D$ at $x < x_\omega$. In other words, the region at $x < x_\omega$ plays the role of an effective flat plate capacitor and defect recharging is irrelevant. However, J_r increases with x at $x > x_\omega$ thus balancing the decay in J_D. Physically, J_D decay is due to screening, while J_r increase follows the number of defects in the region $x - x_\omega$. As x_ω increases with ω, the displacement current region expands and at certain frequency ω_l approaches the geometrical size of the system, $x_\omega = l$ when $E_{\omega_l} = E_F(l)$. At $\omega > \omega_l$ the system is characterized by its geometrical capacitance per unit area $C_g = \epsilon/4\pi l$.

Based on Eq. (4.61) one can calculate the integral admittance as $Y = J_t/U_t$. The shape of $U(x)$ in the integrand of Eq. (4.61) must be preliminary found from Eq. (4.58). However, given the latter shape the admittance can be calculated more easily through the displacement current. Indeed, because $J_r + J_D = const$ and $J_r = 0$ at $x < x_\omega$, Eq. (4.61)

gives the admittance

$$Y = \frac{1}{4\pi U_t} \frac{\partial D(x_\omega - \delta)}{\partial t}\bigg|_{\delta \to 0}. \tag{4.62}$$

Here small δ is introduced to make the equation applicable to a narrow defect band where $D(x)$ changes abruptly, as, for example, described in Eq. (4.59). $D(x_\omega)$ can be expressed by

$$D(x_\omega)x_\omega + \int_{x_\omega}^{l} D(x)dx = \epsilon U_t, \tag{4.63}$$

Eqs. (4.62) and (4.63) together with (4.58) solve the problem of finding the admittance corresponding to a given defect density of states.

Note that the length x_ω remains a parameter in the present consideration. Its value is determined by the static electric field distribution in the system (the barrier shape in Fig. 4.35), which in its turn depends on the defect density of states and external voltage. To calculate x_ω one has to solve the static equation (4.58) for a given defect density of states and Fermi level position. In applications, the inverse problem of calculating the defect density of states based on the impedance measurements is of the major interest. This requires developing a nontrivial numerical algorithm where the frequency dependent impedance data input is used to solve Eqs. (4.62) (4.63), and (4.58) simultaneously for the electric field distribution and defect density of states.

We emphasize the displacement current contribution. In particular, $C_t = (Y_t/i\omega)$ turns out to be different from the differential capacitance $C = dQ/dU$. Indeed, $dQ/dU_t = J_r dt/dU_t = J_r/i\omega U_t$ lacks the displacement current contribution as compared to $C_t = J_t/i\omega U_t$. Experimentally C is found through J_t vs. U_t measurements which include J_D.

Surprisingly, the J_D contribution has been overlooked in the available literature, most of which was based on the dQ/dU_t definition (see the reviews in Refs. 34–36,41). The interpretation in Refs. 42,43 and 44, while utilizing the J_t/U_t approach, does not include J_D either.

Specific cases   In this section we consider three different cases where closed form results can be derived.

Constant density of states

We start with the case of $g(E) = const$, which in Ref. 37 was analyzed based on dQ/dU_t definition. Substituting in Eq. (4.63) $D(x) = D(x_\omega)\exp[-(x - x_\omega)/L]$ to find $D(x_\omega)$ and

using Eq. (4.62) we get

$$Y = \frac{i\omega\epsilon}{4\pi\left\{x_\omega + L - L\exp[(x_\omega - l)/L]\right\}}. \tag{4.64}$$

For $C = \Im(Y/\omega)$ the result has the intuitively clear flat-plate capacitor form. The effective interplate distance is given by the field penetration depth, which is l in the case of weak screening $l - x_\omega \ll L$, or $x_\omega + L$ when the screening is strong. While it has a similar general shape, our result is quite different from that in Ref. 37. In particular, none of the above cited sources, including Ref. 37 gives the geometrical capacitance limit.

Narrow band

The alternative case of a narrow defect band can be approximated by the above discussed $g(E) = N\delta(E - E_\omega)$. Using Eqs. (4.59), (4.63), and (4.62) yields

$$Y = C_g\frac{\omega^2\tau(l - x_\omega) + i\omega[(x_\omega/l) + (\omega\tau)^2]}{(x_\omega/l)^2 + (\omega\tau)^2}. \tag{4.65}$$

This is consistent with the solution of a similar problem in Refs. 35 and 45 far from the geometrical capacitance limit. Our result correctly predicts the geometrical limit in the case of high frequencies where the last term in Eq. (4.65) dominates. Note that a narrow defect band appears to be the only case where the result can be equally calculated based on either J_r or J_D current, since they are spatially separated.

Weak screening

For arbitrary $g(E)$ the problem can be solved analytically in the weak screening limit where $D(x) = \overline{D} + \delta D(x)$ with $\delta D \ll \overline{D} = const$. We approximate $U = \overline{D}(x - l)/\epsilon$ in the right-hand-side of the Poisson equation (4.58) to calculate $\delta D = \overline{D}\int dx(x - l)/L^2$ and find $\overline{D}$ from Eq. (4.63). Close to E_ω we represent $E_F = E_\omega + q\mathcal{E}(E_\omega)(x - x_\omega)$ and use the standard approximation,

$$\frac{1}{1 + i\omega\tau} = \Theta(x - x_\omega) + i\frac{\pi T}{q\mathcal{E}(E_\omega)}\delta(x - x_\omega),$$

where $\Theta(x)$ and $\delta(x)$ are the step-function and delta-function. Assuming smooth $g(E)$ we finally obtain

$$Y = \frac{\pi qT\omega}{\mathcal{E}(E_\omega)l^2}(l - x_\omega)^2 g(E_\omega) \tag{4.66}$$

$$+ i\omega\left[C_g + \frac{q}{l^2}\int_{E_{F,min}}^{E_\omega} dE_F g(E_F)\frac{(l - x(E_F))^2}{|\mathcal{E}(E_F)|}\right].$$

Here $\mathcal{E}(E_F) \equiv dE_F/qdx$ is the static electric field at the point $x(E_F)$ where the Fermi level measured from the band edge is E_F.

For practical purposes, it follows from the above that the uniform field (weak screening) approximation holds when the difference between measured capacitance and its high-frequency value C_g (the frequency-dependent part of capacitance) is relatively small. In particular, a widely used model of additive geometrical and defect-related capacitances fails beyond the weak screening limit.

Conductance - Capacitance Relationship   One direct consequence of Eq. (4.66) is the relationship between the reduced conductance and capacitance

$$\frac{G}{\omega} = -\pi \frac{dC}{d(\ln \omega)}, \tag{4.67}$$

which plays the role of Kramers-Krönig transformation. Based on the above Eqs. (4.56), (4.58), (4.61) one can prove Eq. (4.67) to hold beyond the weak screening case.

Because Eq. (4.67) is specific to the defect contribution it can be used to verify the nature of measured admittance as is illustrated below. Note however that the assumption of smooth $g(E)$ underlying Eq. (4.67) fails for the case of narrow defect band (of the width $\lesssim kT$).
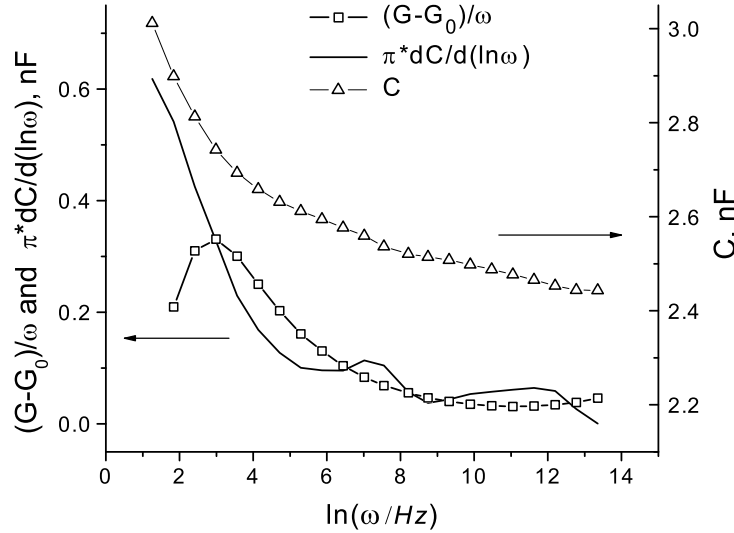

Figure 4.36: Capacitance (C), reduced conductance $[(G - G_0)/\omega]$, and the derivative $\pi dC/d(\ln \omega)$ vs. frequency in CdS/CdTe junction. G_0 is the direct current conductance.

Experimental   Consider the data on thin-film p-n junctions made of 0.3 μm thick CdS (n-type) and 4 μm thick CdTe (p-type) deposited on commercial transparent conductive ox-

66

ide coated glass. A SRS 830 dual-phase digital lock-in amplifier was used in conjunction with a home-built self-calibrating signal-conditioning device. The excitation signal amplitude was about 3.5 mV, frequency range from $\omega_{min} \sim 0.1$ to $\omega_{max} \sim 10^5$ KHz.

Shown in Fig. 4.36 is the measured capacitance for d.c. bias. Defect-related features fall in the domain below 1000 KHz (corresponds to $\ln \omega \approx 9$ in Fig. 4.36) where noticeable frequency dependence is seen. This points at defects with the characteristic relaxation times ranging from 10^{-5} to 100 s. In the high frequency region the measured capacitance corresponds to the flat-plate capacitor with the interplate distance $l \approx 4$ μm consistent with the device thickness.

As is illustrated in Fig. 4.36, our data confirm Eq. (4.67) through almost the entire frequency region, which we consider a strong evidence that the measured admittance features are due to defects. (Minor irregularities in the curve $dC/d\ln \omega$ result from numerical differentiation.) Strong deviation of $dC/d\ln \omega$ from the data in the low frequency region is attributed to a narrow defect band at $E \approx 0.56$ eV as is described by Eq. (4.65). The integral number of active defects can be estimated as $(C(\omega) - C_g)/C_0 \approx 3 \cdot 10^8$ cm^{-2}.

The latter number can be used to estimate the concentration of defects beyond the active band $kT \sim 0.025$ eV. Indeed, based on the observed frequency dependencies in Fig. 4.36, we conclude that defects of comparable density of states occupy the band $B \sim kT \ln(\omega_{max}/\omega_{min})$ of the order of several tenths of the electronvolt, say $B \sim 0.3$ eV. The factor $B/kT \sim 10$ translates the above figure into the integral defect number $N_d \sim 3 \cdot 10^9$ cm^{-2}. Assuming the defects to be uniformly distributed across CdTe film, the corresponding bulk defect concentration $N_d/l \sim 10^{13}$ cm^{-3} is comparable to the known acceptor concentration in CdTe photovoltaics.[46]

Conclusions A general approach to semiconductor device admittance spectroscopy analysis is developed. It describes arbitrary defect distributions, contains the geometrical capacitance limit, and gives the relationship between conductance and capacitance that can be used to test the defect nature of measured admittance. A single defect capacitance concept is introduced that facilitates the analysis. Some experimental verification of our findings is given. From the practical standpoint, our consideration introduces a new diagnostic toolkit that enables one to verify the defect nature of the measured capacitance and calculate the number of active defects.

4.3. Cu K-edge XAFS in CdTe before and after treatment with CdCl$_2$

Introduction   High performance CdS/CdTe thin film solar cells are usually completed with a low resistance Cu back contact. The copper appears to be critical for achieving heavy p-type doping of the CdTe at the contact. It is also known that Cu doping can increase the open-circuit voltage. However, copper is also a fast diffuser,[47] which can accumulate at CdS/CdTe junction and is suspected of playing a role in cell performance deterioration under certain conditions. High-temperature CdCl$_2$ treatment in the presence of oxygen is a critical step needed to improve the performance of CdTe thin-film cells, which can improve the cell efficiency a factor of two or more.[48,49] However the process is not well understood yet. Thus, for this study, samples were prepared through the same processes as completed cells except that the transparent conducting oxide (TCO) and CdS layers were omitted. X-ray absorption fine structure (XAFS) is a powerful technique in materials science research for understanding the lattice environment around designated element atoms, which includes two independent parts: the x-ray absorption near edge structure (XANES) and the extended x-ray absorption fine structure (EXAFS). The XANES is the absorption fine structure spectrum covering the range between the absorption edge of the element itself and the point usually considered to be 50 eV beyond the threshold. And EXAFS cover the region beyond XANES. Also EXAFS is referred to the periodic oscillatory structure in the absorption spectrum above the edge due to the interference between back-scattered and out-going electron waves. Lattice environments are derivable from absorbance spectra by mathematically converting the EXAFS spectrum into a radial distribution function (RDF).

Experimental details   The 2-3 micron CdTe layers were magnetron sputtered at ∼250 ^{o}C, as described in [50], onto either fused silica or Kapton polyimide sheet[51]. All the samples were prepared with 40∼200 Å evaporated Cu layers. Diffusion in N$_2$ at 150 or 200 ^{o}C for at least 45 minutes is applied to all samples. Short 5% hydrochloric acid etchings are also applied to remove the metallic copper left on the film surface. (We found that the x-ray fluorescence from a film with a 200 Å deposited and diffused Cu layer, typically dropped a factor of two after etching. Thus we estimate that about 100 Å of Cu diffused into a 3 μm film. This would imply that the average Cu concentration in a typical film is about 0.3 %.) Some of the samples were annealed at 385 ^{o}C in CdCl$_2$ vapor in a dry air environment for
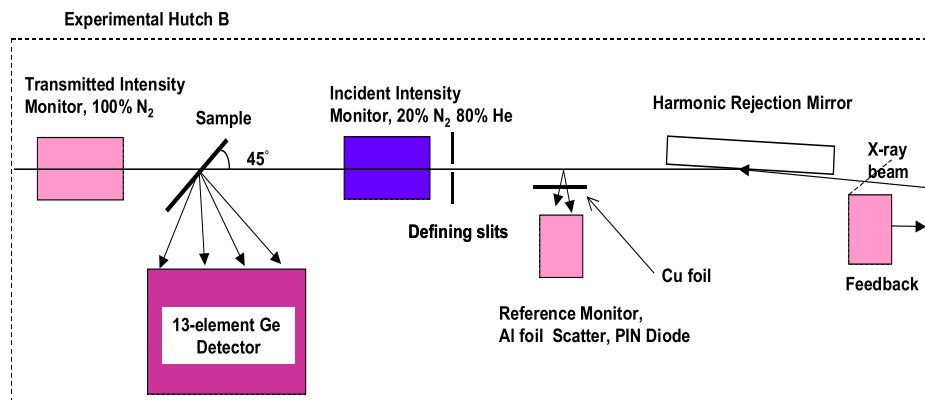
Figure 4.37: Experimental setup at MR-CAT.
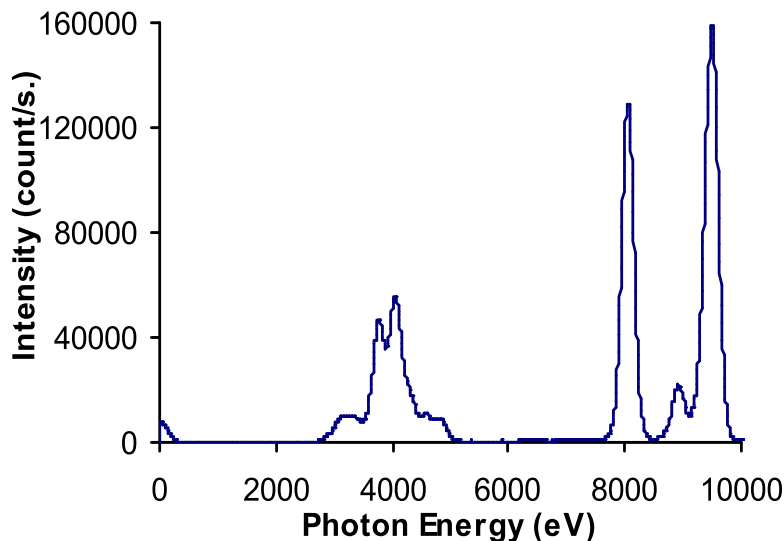
Figure 4.38: X-ray fluorescence spectrum of a Cu-diffused CdTe film excited by 9.5 keV x-ray beam, collected by the 13-element Ge detector.

30 minutes, before Cu deposition, diffusion and etching.

Data were obtained at the Materials Research Collaborative Access Team (MR-CAT) beam-line at the Advanced Photon Source (Argonne IL) with the system shown in Fig. 4.37. The Cu K-edge x-ray absorption spectra of the Cu-doped CdTe samples were collected in a fluorescence geometry with a 13-element high purity Ge detector, by setting a 600 eV wide window at the position of Cu Ka (8048 eV) in the fluorescence spectrum (Fig. 4.38), since

the copper fluorescence intensity is proportional to the absorbance by copper in the thin films. Reference samples of CuO, Cu_2O, $CuCl_2$ and Cu_2Te powders were applied to the adhesive of several layers of Kapton tapes and the absorption spectra were collected in the transmission geometry with detection by Transmitted Intensity Monitor (a N_2 ion chamber).
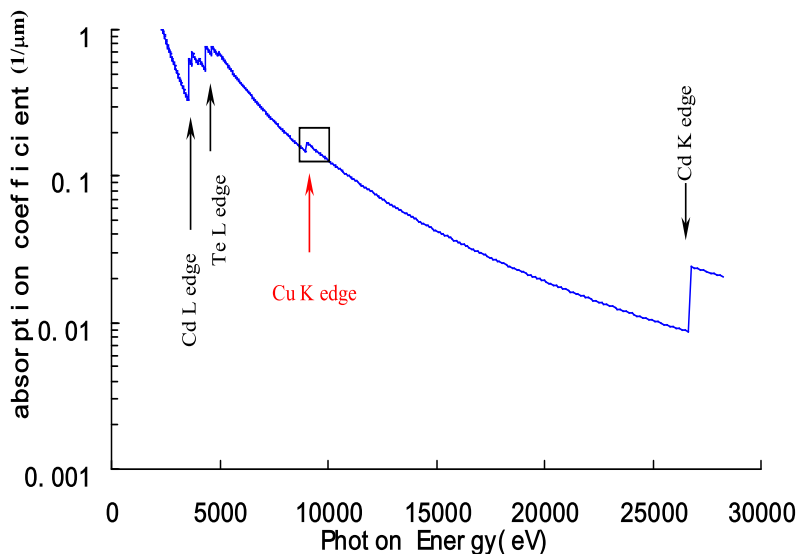
Figure 4.39: Computed x-ray absorption coefficient spectrum of CdTe with 20% Cu[52].

Discussion *Global view of Cu K-edge XAFS*

The computed absorption coefficient for a modeled CdTe film with 20 % Cu is plotted in Fig. 4.39. To check the computation, the actual attenuation coefficient μ of x-ray photons were directly measured by transmission through a series of sputtered CdTe films on polyimide tape, and found to be 0.15, 0.12, and 0.10 μm^{-1} at 8.8, 9.5, and 10.0 keV , agreeing with the computed μ value. Note that our film thicknesses were less than the absorption length. The photon energy range from 8.8 to 10 keV is the same as the one for which XAFS data are collected. Fused silica and polyimide tape were selected to avoid residual heavy elements, such as copper from the soda-lime glass, which might overlap the Cu signal from the CdTe films.

Comparison of XANES spectra

As shown in Fig. 4.40, comparison with reference materials in the XANES region usually helps to understand the predominant chemical bonds surrounding the core atoms in unknown

samples. Before $CdCl_2$ treatment all of the CdTe films are observed to have features similar to Cu_2Te (see Fig 4.40a). However, the films with $CdCl_2$ treatment show features most similar to Cu_2O and CuO (see Fig. 4.40b). Note that the absorption amplitude depends on the sample thickness in direct transmission measurements and depends on detector efficiency and sample thickness for the CdTe: Cu films when fluorescence detection was used. For convenience of comparison, absorption curves in relative magnitude are plotted in Fig. 4.40. The amplitude is not significant in the figure.
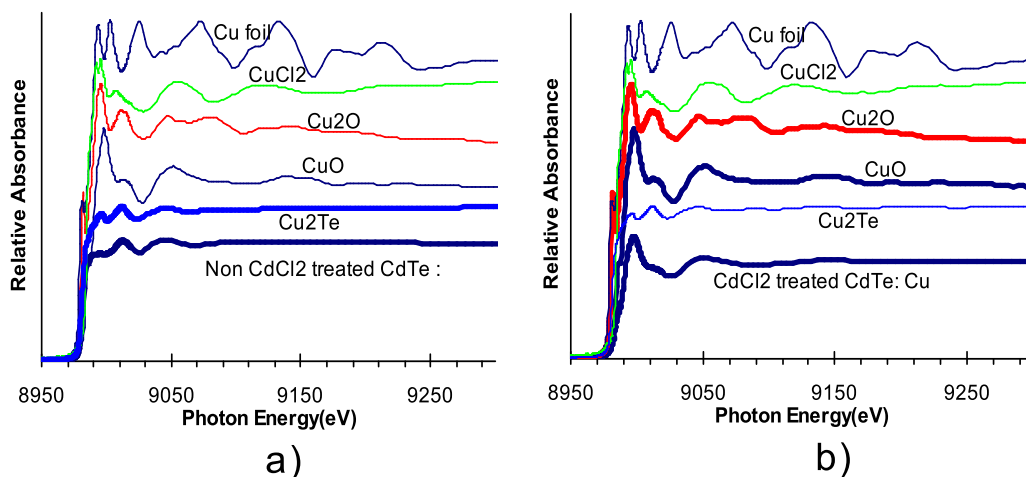
Figure 4.40: X-ray Absorption Near Edge Structure (XANES) spectra. a) Non-chloride treated CdTe films with diffused copper show features similar to Cu_2Te; b) chloride-treated CdTe films with diffused copper show features similar to Cu_2O and CuO.

Data Analysis

EXAFS can be extracted from the x-ray absorption spectra by removing the background. The x-ray absorption backgrounds are calculated as x-ray absorbance in the sample without the electron scattering contribution. Finally the Fourier transform of this fine structure vs. k is the radial distribution function of EXAFS.[53] Our analyses were performed through IFEFFIT an interactive program for XAFS analysis.[54]

The radial distribution functions for the two cases–without $CdCl_2$ treatment and with $CdCl_2$–are shown in Fig. 4.41. In the RDF of Fig. 4.41a, we also observe that the peak of the first nearest neighbor at 2.42 Å shifts to a shorter distance by about 0.1 Å than the one in cuprous telluride, but otherwise there is a strong correspondence. We are still studying the data and analysis to determine whether this shift is real. The magnitude in FT mostly

Figure 4.41: Radial Distribution Function after Fourier Transform.

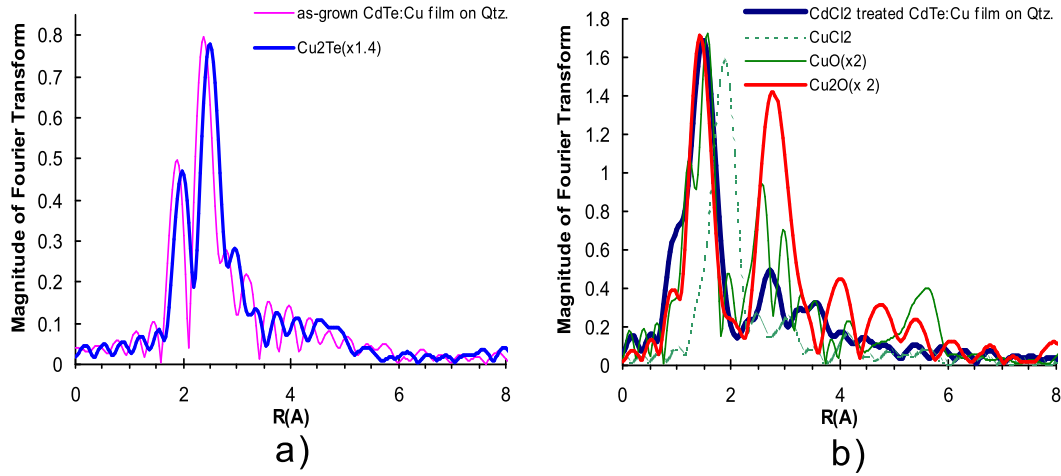depends on the coordination number in the neighbor shell. Without further theoretical modeling, we are not able to fully interpret the difference of the FT magnitudes of various peaks.

For the $CdCl_2$ treated films, the shape of the RDF and the position of the peaks are substantially changed. Thus, we infer that the chemical environment of the typical copper atom is substantially changed. The peak of the first nearest neighbor resides at a position neither the same as cuprous telluride, Cu_2Te, nor cupric chloride, $CuCl_2$, but corresponds closely to cuprous oxide, Cu_2O at 1.50 Å, as shown in Fig. 4.41b. Although the XANES spectra (Fig. 4.40b) show features similar to CuO in the Cl-treated film, the RDF does not prove the existence of CuO in the film. Since the second nearest neighbors of copper in cuprous oxide are copper atoms,[55] the fact that the second nearest neighbor peaks in Fig. 4.41b, are very different suggests that we are not seeing nanocrystal inclusions of cuprous oxide but rather copper-oxygen clusters formed in the film or quite likely along the grain boundaries.

Discussion

Our films were diffused with a typical concentration of copper of about 0.3% or an average density of 1-2 x 10^{20} cm^{-3}. However, capacitance-voltage (C-V) measurements on typical CdTe solar cells, including our sputtered cells indicate a typical doping concentration of holes of a few times 10^{14} cm^{-3}.[56] Secondary ion mass spectroscopy (SIMS) on some CdTe cells has shown Cu atomic concentrations of a few times 10^{19} cm^{-3}.[57] Our preparation of films

was done with evaporated Cu amounts only slightly higher than we use for cell fabrication. Clearly much Cu is not active as an acceptor in these films and there is considerable interest in the environment of non-electrically active Cu. Based on our x-ray absorption fine structure measurements, we conclude that the answer depends entirely on whether the film has received the typical treatment with $CdCl_2$. Thus, films which received the Cu diffusion having no prior treatment with $CdCl_2$ appear to show the Cu mostly bound with Te similar to Cu_2Te. *However*, if the film had received the $CdCl_2$ treatment, *which for cells is always done in the presence of some O_2*, then the Cu appears to be bound not with Cl but with O. The most plausible interpretation is that most of the copper was available at grain boundaries where it could easily be oxidized in an oxidization environment prepared by the prior $CdCl_2$ treatment. It is generally understood that this $CdCl_2$ treatment is important for passivating the grain boundaries and thus is a critically important step in the fabrication of high efficiency polycrystalline thin-film solar cells. These x-ray absorption fine structure measurements point toward a plausible interpretation of this chloride treatment as well as other observations that the preparation of a Te-rich surface (e.g., by chemical etching with Br_2/methanol or HNO_3/H_3PO_4[58]) is often important for fabricating high efficiency cells. The wider band-gap cuprous oxide on the CdTe grain boundaries may prevent the recombination of electron-hole pairs there.[59] However, more information on band lineups between Cu_2O and CdTe will be needed to confirm that this is a plausible interpretation.

Fitting to theoretical standards derived from the ab initio multiple-scattering code FEFF[60] is in progress to obtain more detailed information about the near-neighbor distance and the coordination numbers of the environment surrounding the copper atoms.

4.4. Low light divergence in the fluctuations of photovoltaic parameters

We have studied statistics of the major photovoltaic (PV) parameters such as open circuit voltage, short circuit current, etc. vs. light intensity on a set of nominally identical thin-film CdTe/CdS solar cells. A crossover light intensity is found, below which the relative fluctuations of the PV parameters diverge inversely proportional to the square root of the light intensity. More specifically,

$$\frac{\delta J_{sc}}{J_{sc}}, \frac{\delta V_{oc}}{V_{oc}}, \frac{\delta\left(FF\right)}{FF} \propto \begin{cases} I^{-1/2} & \text{for} \quad I < I_c, \\ const & \text{for} \quad I > I_c. \end{cases} \tag{4.68}$$

From the practical standpoint, our study introduces a simple uniformity diagnostic technique.
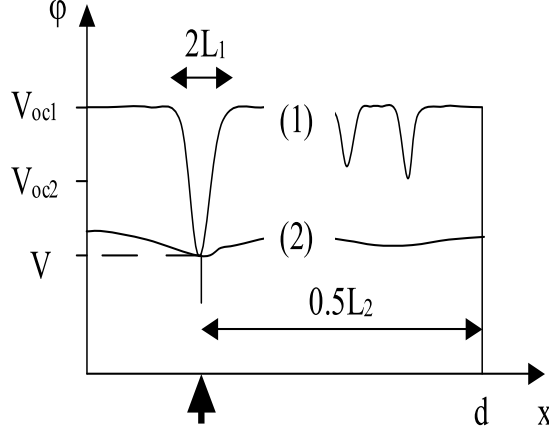

Figure 4.42: Electric potential distribution along the resistive electrode, which is the TCO for the standard cells and 5 nm Cr contact for the high resistive electrode cells. The measuring probe (fat arrow) applies voltage bias V. The cases of (1) small and (2) large L/l are shown. For illustration purposes, the cell is uniform to the left of the probe and nonuniform to the right of it. In the case (1) the nonuniformities are screened ($L_1 \ll d$) and do not affect the current collection, as opposed to the case (2) where they compete for the current with the probe ($L_2 \gg d$).

To explain Eq. (4.68) we proceed from the fact that a point lateral nonuniformity causes the electric potential scaling as $V(r/L)$ with the coordinate r. The corresponding microcurrent then becomes $\delta j \propto \nabla V \propto L^{-1}$. When $L/d \ll 1$, the current fluctuation felt by the probe is $\delta J \approx \delta j \sqrt{N} \propto L^{-1} L^{D/2} \propto I^{(D-2)/2}$, where $N \sim L^D$ is the number of shunts (weak diodes) in the active domain $\sim L^D$ (see Fig. 4.42). In the mean time, as is also seen from Fig. 4.42, the average short-circuit current, $J_{sc} \approx V_{oc}/\rho$ is logarithmic in intensity, simply following $V_{oc} \propto \ln J_{sc}$. As a result, the relative current fluctuation $\delta J_{sc}/J_{sc} \propto I^{(D-2)/2}$ is practically independent of the light intensity when $L/d \ll 1$ and D=2. In the low light regime, $L/d \gg 1$ the number of shunts N does not depend of L and is determined by the entire device area, while J_{sc} is proportional to the light intensity. Incorporating these changes yields $\delta J_{sc}/J_{sc} \propto 1/LI \propto 1/\sqrt{I}$. The crossover intensity I_c between the two regimes is determined by the condition $L = d$. (Note that in the 1D

74

case the divergency $\sim I^{-1/2}$ holds both for $L \ll d$ and $L \gg d$.) It is straightforward to
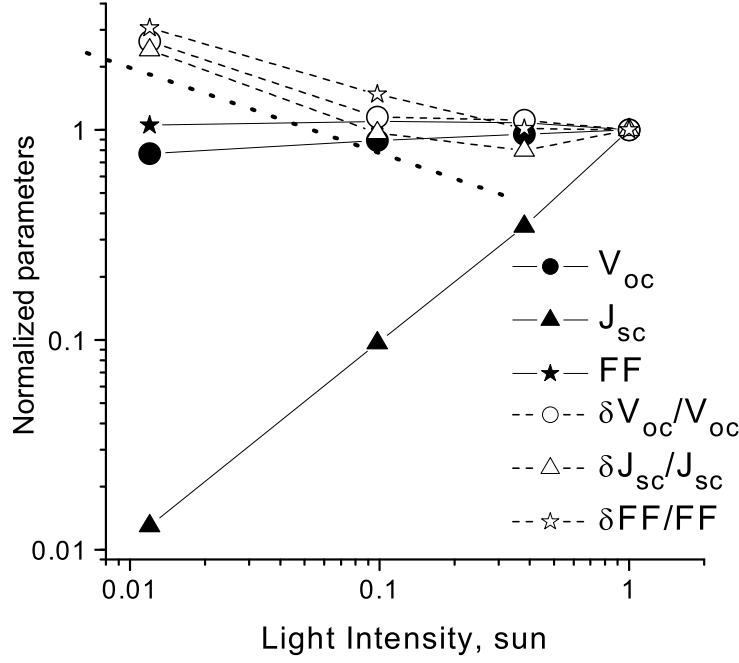

Figure 4.43: The average PV parameters open-circuit voltage V_{oc}, short-circuit current J_{sc} and fill factor FF (solid symbols and lines), and their relative standard deviations (open symbols, dashed lines) versus light intensity normalized to the respective values at 1 sun and measured for an ensemble of 130 vapor transport deposited cells. Note the logarithmic scale: the standard deviations increase by a factor of 3 as the light intensity decreases by a factor of 10. The dotted line shows the predicted slope of the light intensity to the power -0.5.

extend the above reasoning to the parameters V_{oc} and FF. Because $V_{oc} \propto \ln J_{sc}$, one gets $\delta V_{oc}/V_{oc} \propto \delta J_{sc}/\left(J_{sc} \ln J_{sc}\right) \sim \delta J_{sc}/J_{sc}$. The fill factor is sensitive to both the current and the potential (although the exact dependence is not known). In the first approximation one can write $\delta FF/FF \sim \delta J_{sc}/J_{sc} + \delta V_{oc}/V_{oc}$. Thus, the relative fluctuations in V_{oc} and FF depend on the light intensity similarly to that of J_{sc} and the FF relative fluctuation is roughly twice as large as the other two.

To verify the prediction in Eq. (4.68) we studied fluctuations in the main PV parameters of 180 standard CdS/CdTe cells (efficiencies in the range of 10%) made by vapor-transfer deposition as described in Ref. 23. These cells are thin-film junctions sandwiched between two roundish (D=2) electrodes (area 1.1 cm^2), of which one is the TCO with sheet resistance $\rho = 15\Omega/\square$ and the other is a metal layer of negligibly small resistance. Our results in Fig.

4.43 are in excellent agreement with Eq. (4.68). Our estimate for the crossover intensity $I_c \sim 0.1$ sun is consistent with the observations when we take $L \sim L_0$. We have also verified that the relative fluctuations in FF are roughly twice as large as that in J_{sc} and V_{oc}.

References

[1] Diana Shvydka, V. G. Karpov, and A. D. Compaan, Appl. Phys. Lett. **80**, 3114 (2002).

[2] James Ziegler, SRIM, the Stopping and Range of Ions in Matter, http://www.srim.org/.

[3] V.D. Popovich, G.M. Grigorovich, P.M. Peleshchak, and P. N. Tkachuk, *Semiconductors*, **36**, No. 6, pp. 636-640, 2002

[4] P. Siffert, A. Cornet, R. Stuck, R. Triboulet, Y. Marfaing, *IEEE Trans. Nucl. Sci.* NS-22 (1975) 211.

[5] R.O. Bell, F.V. Wald, C. Canali, F. Nava, G. Ottaviani, *IEEE Trans. Nucl. Sci.* NS-21 (1974) 331.

[6] N.V. Agrinskaya, E.N. Arkadeva, *Nucl. Instr. and Meth.* **A 283** (1989) 260.

[7] D. M. Hofmann, P. Omling and H. G. Grimmeiss, *Phys. Rev. B*, **45**, 11, 6247-50, 1992.

[8] T. Schmidt and K. Lischka, *Phys. Rev. B*, **45** (1992) 8989-94.

[9] D.V. Korbutyak, S.G. Krylyuk, P.M. Tkachuk, V.I. Tkachuk, N.D. Korbutak, *J. Cry. Gr.*, **197** (1999) 659-662.

[10] S-H. Wei, S.B. Zhang, and A. Zunger, *J. Appl. Phys.* **87**, 1304 (2000).

[11] R.A. Street, Phys. Rev. B **17**, p.3984 (1978).

[12] T. N. Mamontova and A. V. Chernyshev, Soviet Physics - Semiconductors **18**, 332 (1984).

[13] D. Guidotti, Eram Hasan, H.J. Hovel, and Marc Albert, Appl. Phys. Lett. **50**, 912 (1987).

[14] M.Y.A. Raja, S.R.J. Brueck, M. Osinski, and J. McInerney, Appl. Phys. Lett. **52**, 625 (1988).

[15] D. Guidotti and H.J. Hovel, Appl. Phys. Lett. **53**, 927 (1988).

[16] D. Guidotti and H.J. Hovel, Appl. Phys. Lett. **53**, 1411 (1988).

[17] Bosang Kim, I. Kuskovsky, Irving P. Herman, D.Li, and G.F. Neumark, J. Appl. Phys. **86**, 2034 (1999).

[18] R. Laiho, A. Pavlov, and O. Hovi, T. Tsuboi, Appl. Phys. Lett. **63**, 275 (1993).

[19] I. M. Chang, S. C. Pan, and Y. F. Chen, Phys. Rev. B **48**, 8747 (1993).

[20] G.M Haugen, S. Guha, H. Cheng, J.M. DePuydt, M.A. Haase, G.E. Hofler, J. Qiu, and B.J. Wu, Appl. Phys. Lett. **66**, 358 (1995).

[21] R.Harju, V.G. Karpov, D. Grecu, and G. Dorer, J. Appl. Phys. **88**, 1794 (2000).

[22] D. H. Levi, L. M. Woods, D. S. Albin, T. A. Gessert, R. C. Reedy, and R. K. Ahrenkiel, in *Proceedings 2d World Conference on Photovoltaic Solar Energy Conversion*, Vienna, Austria (1998), available at www.nrel.gov/ncpv/pdfs/levi.pdf.

[23] Diana Shvydka, A. D. Compaan and V. G. Karpov, J. Appl. Phys. **91**, 9059 (2002).

[24] Bolko von Roedern, Mat. Res. Soc. Symp. Proc. **668**, p.H6.9.1 (2001).

[25] D. Redfield and R. Bube, *Photoinduced Defects in Semiconductors*, Cambridge, University Press 1996.

[26] V. G. Karpov, A. D. Compaan, and Diana Shvydka, Appl. Phys. Lett. **80**, 4256 (2002).

[27] The derivative estimate is valid since the length $\alpha^{-1} \approx 0.3$ μm is much shorter than the characteristic drift and diffusion lengths ($\sim 1 \div 3$ μm) in the material.

[28] H. Sher and T. Holstein, Phil. Mag., **B**, **44**, 343 (1981).

[29] S.M. Sze *Physics of Semiconductor devices*, John Wiley and Sons, New York, 1981.

[30] J.F. Hiltner and J.R. Sites, *Proceedings AIP Conf.* **462**, 170 (1998).

[31] S. S. Hegedus, B. E. McCandles, and R. W. Birkmire, *Proceedings 28th IEEE Photovoltaic Specialists Conference*, Alaska, 2000, p. 535.

[32] Our consideration does not describe degradation under significant reverse bias, which mechanism can be different (for example, electromigration or localized charge carrier generation through the Frantz - Keldysh effect).

[33] Linear rescaling was performed in such a way, that initial and final data points were superposed for all three degradation curves. In particular, the final relative degradation in Fig. 4.33 does not show the actual efficiency and EBIC (electron beam induced current) degradation absolute values.

[34] D. K. Schroder, *Semiconductor Material and Device Characterization*, John Wiley, 1998.

[35] P. Blood and J. W. Orton, *The electrical characterization of semiconductors: majority carriers and electron states*, Academic Press, NY 1992.

[36] J. D. Cohen, *Semiconductors and Semimetals* **21**, Part C, Editor J. I. Pankove, 9 (1984).

[37] I. G. Gibb and A. R. Long, Phil. Mag. B **49**, 565 (1984).

[38] J. D. Jackson, *Classical Electrodynamics*, John Willey, New York, 1975.

[39] N. F. Mott and E. A. Davis, *Electron Process in Non-Crystalline Materials*, Clarendon Press, Oxford, 1979.

[40] Because L has imaginary part, $U(x)$ in general, oscillates. This may be important for the flat band case, for example, determining quasistationary field propagation in amorphous solids. Band bending ($0 < x_\omega < l$) suppresses the oscillations, since $\omega\tau \ll 1$ in practically important region $x > x_\omega$.

[41] I. Balberg, *J. Appl. Phys.* **58**, 2621 (1986).

[42] T. Walter, R. Herberholz, C. Muller, and H. W. Schock, *J. Appl. Phys.* **80**, 4411 (1996).

[43] J. Kneisel, K. Seimer, and D. Brauning, *J. Appl. Phys.* **88**, 594 (2000).

[44] A. Jasenek, U. Rau, V. Nadenau, and H. W. Schock, *J. Appl. Phys.* **87**, 5474 (2000).

[45] P. Krispin, *Appl. Phys. Lett.* **70**, 1432 (1997).

[46] T. J. McMahon and A. L. Fahrenbruch, *Proc.* 28 *th IEEE Photovoltaic Specialists Conference*, Alaska, p. 539 (2000).

[47] H.C. Chou, A. Rohatgi, N.M. Jokerst, E.W. Thomas, S. Kamra, *J. Electron. Mater.* **25**, 1093 (1996).

[48] P. V. Meyers, C. H. Liu, T. J. Frey, U.S. Patent 4,710,589 (1987).

[49] R. W. Birkmire, B. E. McCandless and S. S. Hegedus, *Int. J. Sol. Energy*, **12**, 145 (1992); And S. A. Ringle, A. W. Smith, M. H. Macdougal and A. Rohatgi, *J. Appl. Phys.*, **70**, 881 (1991).

[50] A.D. Compaan *Mat. Res. Soc. Symp. Proc.*, **763**, B3.7.1, 2003.

[51] http://www.dupont.com/kapton/

[52] Data were converted from the computed result obtained from Center for X-Ray Optics at E. O. Lawrence Berkeley National Lab, http://www-cxro.lbl.gov/optical_constants/atten2.html.

[53] D. C. Koningsberger and R. Prins, *X-ray Absorption: Principles, Applications, Techniques of EXAFS, SEXAFS and XANES*, John Wiley & Sons, New York, 1988 .

[54] Developed by Matte Newville, http://cars9.uchicago.edu/ifeffit/.

[55] Ralph W. G. Wyckoff, *Crystal Structures*, John Wiley & Sons, New York, 1963.

[56] A.O. Pudov, M. Gloeckler, S.H. Demtsu, 29 *th IEEE Photovoltaic Specialists Conference*, pp. 760-3, IEEE, Piscataway, N.J., 2002.

[57] S.E. Asher, F.S. Hasoon, T.A. Gessert, 28 *th IEEE Photovoltaic Specialists Conference*, pp 479-482, IEEE, Piscataway, N.J., 2000.

[58] B.E. McCandless, J.E. Phillips and J. Titus, *2nd World Conference on PV Solar Energy*, Vi-

enna, Austria, 1998, pp 448-452.

[59] T. R. Ohno, Eli Sutter, James M. Kestner, A. S. Gilmore, H6.5, *Spring Mat. Res. Soc. Symp.*, (2001).

[60] The FEFF Project, Department of Physics, University of Washington, Seattle, WA, http://leonardo.phys.washington.edu/feff/.

5. PUBLICATIONS

5.1. Refereed papers published or in press (9/1/02 - 8/31/03)

1. "All sputtered 14% CdS/CdTe device with ZnO:Al front contact", Akhlesh Gupta and Alvin. D. Compaan, Proceedings of 3rd World Conference on Photovoltaic Energy Conversion, May 11-18, 2003, Osaka, Japan (to be published).

2. "Oxygenated CdS window layer for sputtered CdS/CdTe solar cells", Akhlesh Gupta, Karthikeya Allada, Sung Hyun and Alvin. D. Compaan Compound Semiconductor Photovoltaics, edited by Rommel Noufi, William N. Shafarman, David Cahen and Lars Stolt, Mat. Res. Soc. Symp. Proc. 763, B8.9 (2003).

3. "14% CdS/CdTe solar cell with ZnO:Al TCO", Akhlesh Gupta and Alvin D. Compaan ,Compound Semiconductor Photovoltaics, edited by Rommel Noufi, William N. Shafarman, David Cahen and Lars Stolt, Mat. Res. Soc. Symp. Proc. 763, B3.9 (2003).

4. "Cu K-edge XAFS in CdTe before and after treatment with $CdCl_2$", Xiangxin Liu, A. D. Compaan, Nadia Leyarovska, and Jeff Terry, Compound Semiconductor Photovoltaics, edited by Rommel Noufi, William N. Shafarman, David Cahen and Lars Stolt, Mat. Res. Soc. Symp. Proc. 763, B3.5 (2003).

5. "Admittance spectroscopy revisited: Single defect admittance and displacement current", V. G. Karpov, Diana Shvydka, U. Jayamaha and A. D. Compaan, J. Appl. Phys. **94**, 5809 (2003).

6. "Photoluminescence Fatigue and Related Degradation in Thin-Film Photovoltaics", Diana Shvydka, C. Verzella , V. G. Karpov and A. D. Compaan, J. Appl. Phys. **94**, 3901 (2003).

7. "Photoluminescence fatigue in CdTe photovoltaics", Diana Shvydka, C. Verzella and V. G. Karpov, Compound Semiconductor Photovoltaics, edited by Rommel Noufi, William N. Shafarman, David Cahen and Lars Stolt, Mat. Res. Soc. Symp. Proc. 763, B5.7 (2003).

8. "Low Light Divergence In Photovoltaic Parameter Fluctuations", Diana Shvydka, V. G. Karpov and A. D. Compaan, Appl. Phys. Lett. **82**, 2157 (2003).

9. "The mesoscale physics of large-area photovoltaics", V. G. Karpov, Diana Shvydka, Yann Roussillon, and A. D. Compaan, Proceedings of 3d World Conference on Photovoltaic Energy Conversion, May 11-18, 2003, Osaka, Japan (to be published).

5.2. Poster or oral presentations published on CDROM and the NREL Web site

1. "Thermography Mapping and Modeling", Diana Shvydka, J.P. Rakotoniaina and O. Breitenstein, National CdTe R&D Team Meeting; FSEC, Golden, CO; July 10-11, 2003.

2. "Photoluminescence Mapping", Diana Shvydka, A. D. Compaan and V. G. Karpov, National CdTe R&D Team Meeting; FSEC, Golden, CO; July 10-11, 2003.

3. "Low-light diagnostics" Diana Shvydka, A. D. Compaan and V. G. Karpov, National CdTe R&D Team Meeting; FSEC, Golden, CO; November 28-29, 2002.

5.3. Contributed oral or poster presentations (no published manuscript)

1. "Low Light Diagnostics in Thin-Film Photovoltaics", Diana Shvydka, V.G Karpov, A.D. Compaan, APS March meeting, Austin, TX, March 3-7, presentation A8.002, 2003.

2. "A new class of disordered systems: large-area electronics", V. G. Karpov, A. D. Compaan, and Diana Shvydka, APS March meeting, Austin, TX, March 3-7, presentation B15.014, 2003.

3. "Cu K-edge EXAFS in CdTe before and after treatment with $CdCl_2$", Xiangxin Liu, A. D. Compaan, Nadia Leyarovska, and Jeff Terry, 3rd Conference Thin Film and Nanotechnology for Energy Conversion and Storage, Cleveland, OH, September 18-19, poster A3, 2003.

4. "Nonuniformuties and photovoltaic self healing", Yann Roussillon, D.M. Giolando, Diana Shvydka, A.D. Compaan, and V.G. Karpov, 3rd Conference Thin Film and

Nanotechnology for Energy Conversion and Storage, Cleveland, OH, September 18-19, poster C5, 2003.

5. "Modulated PL in CdS/CdTe solar cells", A.C. Vasko, S. Hickman, and A.D. Compaan, 3rd Conference Thin Film and Nanotechnology for Energy Conversion and Storage, Cleveland, OH, September 18-19, poster C6, 2003.

5.4. Annual Subcontract Reports Summary published in U.S. Dept. of Energy Photovoltaic Energy Program Contract Summary, FY 2002

A.D. Compaan and V.G. Karpov, "The Fabrication and Physics of High Efficiency Cadmium-Telluride Thin-Film Solar Cells."

6. PROJECT PERSONNEL

6.1. Research professor

Akhlesh Gupta (Ph.D. Indian Institute of Technology, Delhi)(50% time, 9/1/01–)

6.2. Postdoctoral Associates

Shanli Wang (Ph.D. Shanghai Inst. Of Technical Physics, 97)(50% time, 6/02–)
Diana Shvydka (Ph.D., U. of Toledo, 5/2002)(9/02–)

6.3. Graduate Students (with Principal Advisor)

(Some students received support from other sources but made significant contributions to this work)

Jennifer Drayton (Compaan)
>   Ph.D. in progress

Xiangxin Liu (Compaan)
>   M.S. and Ph.D. in progress

Yann Roussillon (Giolando)
>   Ph.D. in progress

Todd Osborn (Giolando)
>   M.S. and Ph.D. in progress

Anthony Vasko (Compaan)
>   M.S. and Ph.D. in progress

Viral Parikh (Compaan)
>   M.S. and Ph.D. in progress

Karthikeya Allada (Compaan)

        M.S. and Ph.D. in progress

6.4. Undergraduate students

Levi Gorrell (Karpov), during Summer 2003

NSF Research Experiences for Undergraduates (REU), Summer 2003:
Samantha Dizor (Karpov), "Photoluminescence Fatigue in CdTe/CdS Solar Cells"

6.5. Technical Assistants

Terry Kahle (3/03–)

Robert Burmeister (4/96–) (25% time)